Materials & Design 226 (2023) 111641

Contents lists available at ScienceDirect

Materials & Design

journal homepage: www.elsevier.com/locate/matdes

Additively manufactured three-dimensional lightweight cellular solids: Experimental and numerical analysis

Albert Forés-Garriga, Giovanni Gómez-Gras, Marco A. Pérez *

IQS School of Engineering, Universitat Ramon Llull, Via Augusta 390, 08017 Barcelona, Spain

HIGHLIGHTS

- 3D cellular designs exhibit an improved and more isotropic mechanical performance than 2D patterns at similar levels of density.
- Although most of the 3D designs require support structures for their manufacturing, no increase in building time is noticed.
- The implementation of the sparse infill saves material, weight and printing time, while performance is slightly impacted.
- A novel and more consistent method for quantifying the isotropy of cellular solids fabricated with additive manufacturing technologies is provided.
- The homogenized numerical approach employing representative volume element properties saves important computation time with enough accuracy.

GRAPHICAL ABSTRACT

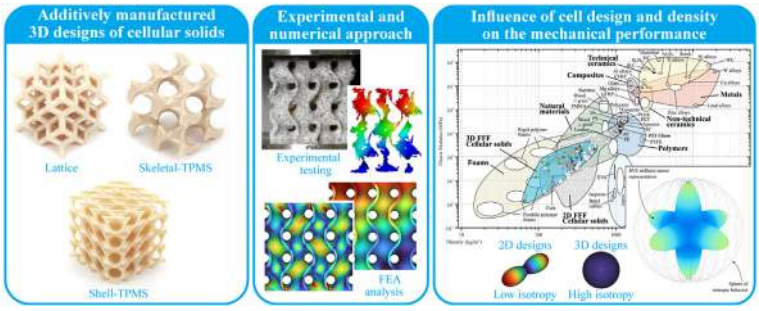

ARTICLE INFO

Article history:
Received 17 July 2022
Revised 16 January 2023
Accepted 17 January 2023
Available online 21 January 2023

Keywords:
Fused filament fabrication
Triply periodic minimal surfaces
Lattice
Material properties
Finite element analysis
Homogenization

ABSTRACT

The development of cellular solids is one of the research fields in which additive manufacturing has made relevant progress in producing lightweight components and enhancing their performance. This work presents comprehensive research on the mechanical performance of fused filament fabricated three-dimensional lightweight cellular solids, including open-cell and closed-cell lattice designs and triply periodic minimal surfaces (TPMS), with different cell sizes and infill densities. The aim of this work is to determine the range and limits of the achievable mechanical behavior by employing different cell designs made from a single material and manufacturing technique. Experimental results obtained with cell designs fabricated with a high-performance polymer (PEI Ultem) showed wide ranges of effective stiffnesses from 1 to 293 MPa, strengths from 0.1 to 18.1 MPa, and densities from 0.066 to 0.541 g/cm^3. Furthermore, two validated numerical approaches are provided to simulate their mechanical performance accurately. Moreover, a novel and robust index to quantify the isotropy of additively manufactured cellular solids based on the graphical representation of the homogenized stiffness tensor is proposed. Finally, experimental evidence states that the Shell-TPMS designs proved to be the most efficient cellular pattern, followed by the Skeletal-TPMS and the lattice configurations.

* Corresponding author.
E-mail address: marcoantonio.perez@iqs.url.edu (M.A. Pérez).

https://doi.org/10.1016/j.matdes.2023.111641
0264-1275/

1. Introduction

Additive manufacturing (AM) has attracted enormous attention from the scientific community and different industrial sectors in the last decade. It undoubtedly constitutes one of the strategic pillars of the global transformation towards Industry 4.0. Moreover, the rapid transition between research developments and industrial applications has been consolidated due to the ability to fabricate functional parts with complex geometries, which are unfeasible to obtain using conventional manufacturing techniques.

In particular, one of the research fields in which AM has made relevant progress is the development and manufacturing of cellular solids [1–4]. These bio-inspired structures are formed by a complex interconnected network of solid struts or shells that cover the space while considerably reducing the weight of the components [5–7]. Depending on the unit cells' typology and arrangement, cellular solids can be classified into two principal categories: closed-cell designs, such as foams, or open-cell ones, composed of reticular microstructures, such as lattices [8]. The properties of these cellular solids directly depend on the shape and connectivity of the unit cells and the solid material used for their manufacturing [9,10]. Thus, this advanced and optimized microarchitecture gives them properties of great interest and applicability, such as rigidity and specific resistance, thermal and acoustic insulation, or impact absorption capacity [11–21].

Some of these designs have already been incorporated into 3D printing equipment as an infill method for parts construction, with the aim to reduce manufacturing time and costs associated with material consumption [22]. However, an advanced design of cellular solids demands tight control of the kinematics of their deformation to achieve the desired microstructure properties to satisfy specific design requirements [23–31]. Therefore, a better understanding of the structure's behavior allows for finer control of mechanical properties [32,33]. Hence, architectural cellular materials are very versatile, as their performance can be tailored by simply modifying the geometrical or topological parameters of the design. Thus, according to the vast literature published in the last five years, it can be stated that there is an interest in the scientific community in deepening the knowledge, development, and fabrication of these bio-inspired microstructures for their application in advanced structural components.

Previous research has demonstrated that specific AM techniques are better suited for manufacturing certain typologies of cellular solids. In particular, the fabrication of lattice-type arrangements often requires intensive use of support structures. In this sense, employing powder bed technologies avoids the fabrication of supports, since the whole powder volume sustains the following constructed layer [34–41]. Therefore, powder bed fusion (PFB) is the most used technique for manufacturing truss-like cellular solids [42–48]. On the other hand, fused filament technologies deposit a thermoplastic material layer by layer according to the trajectories of a moving extruder head. Therefore, studies employing fused filament fabrication (FFF) generally deal with cell geometries composed of shell-like walls, as the vertical overlapping of the deposited rasters favors the construction of honeycomb-like designs [49–51]. Nevertheless, its implementation in manufacturing lightweight three-dimensional structures, such as lattice designs, requires removable auxiliary supports to hold inclined walls or struts during their construction.

In spite of this shortcomings, FFF stands as the most accessible, cost-effective, fastest, and user-friendly technique compared to the rest of the AM technologies. Moreover, its benefits for constructing two-dimensional cellular solids have been sufficiently consolidated [52,53]. However, the extrusion plane present in all of these designs significantly increases the degree of anisotropy of the structures, which exhibit a maximum in-plane stiffness while dramatically compromising the perpendicular one [54]. On the contrary, this phenomenon does not appear in three-dimensional designs, which leads to higher degrees of isotropy [55]. For this reason, many authors have recently focused on exploring the capabilities of this technology to manufacture three-dimensional structures using a much more economical and sustainable process [56–58].

One of the most promising developments in three-dimensional cellular solids for lightweight applications are the called triply periodic minimal surfaces (TPMS) [59,60]. These geometries are mathematically created to minimize the surface area for a given volume, having no self-intersecting or enveloping surfaces. Moreover, the lack of nodes and discontinuities in their curvature reduces stress concentration, thus improving their mechanical performance [61,62]. In addition, the average curvature at each point of the geometry is zero, hence making them self-supporting and able to be fabricated by FFF without requiring support structures [52,63–66].

Despite the high interest in cellular solids several uncertainties remain, especially for employing them in high-performance structural applications, such as composite material sandwich structures. Thus, and taking advantage of the most recent developments in AM technologies, these designs can become a turning point for obtaining novel lightweight cores with more isotropic and customized properties.

Accordingly, this work investigates the mechanical performance of FFF three-dimensional cellular solids to comprehend their benefits over two-dimensional designs in terms of stiffness and strength while attending manufacturing aspects such as printing time. The aim of this work is to explore the capabilities of cellular solids to achieve, from a single high-performance polymeric material, very different mechanical behaviours that allow broad applicability of this lightweight structures by customising only the cell design. In order to do so, the compressive behavior of twenty designs, including both open-cell and closed-cell patterns with different cell sizes and infill densities, is experimentally analyzed. In contrast to some previously published works, this study is conducted using professional FFF equipment, which incorporates a heating chamber to improve the cohesion between layers and increase the stiffness of the joints of the melted material. Furthermore, to inspect the structural capabilities of each design, a high-performance technical polymer with an outstanding strength-to-weight ratio is used. Additionally, the isotropy of the manufactured cell type is evaluated by employing a numerical homogenization strategy. Lastly, two validated numerical approaches are provided to efficiently simulate the compression and bending response of cellular designs, further contributing to novel design-for-manufacturing strategies of lightweight cores for sandwich structures.

2. Methodology

2.1. Manufacturing of the samples

A total of 20 different three-dimensional cellular solids were selected to analyse the impact that both the unit cell geometry and the relative density may have on the mechanical performance and manufacturing feasibility (see Fig. 1 and Table 1). For simplicity, from now on, pattern names and specimen identifications are referenced with the corresponding ID. Although FFF might be an unconventional choice for manufacturing certain geometries, this work comprises the study of all typologies of three-dimensional cellular solids, including lattice (*A* to *H*), Skeletal-TPMS (*I* to *O*), and Shell-TPMS (*P* to *T*).

Fig. 1. Unit-cells (Specimen ID_1) and eight-cells (Specimen ID_8) samples of the three-dimensional patterns manufactured with FFF (see Table 1).

Lattice geometries have been created using SolidWorks. On the other hand, the novel TPMSgen [67] open-source Python application was developed to parametrically generate the Skeletal-TPMS and Shell-TPMS designs employing the corresponding equations (see Appendix A). In each case, a cubic volume of 40 mm of side length was covered using two different unit cell sizes (I: $40 \times 40 \times 40$ mm; II: $20 \times 20 \times 20$ mm), thus resulting in structures made of a single cell (Specimen ID_1) and others of eight cells

Table 1
Pattern ID, manufacturing time, and relative density of the analyzed three-dimensional cellular solids.

Pattern (see Fig. 1)	Family ID	Typology	Specimen ID	Solid ± 45° Infill		Sparse 0.25 mm Infill		
				Manufacturing time (min)	Relative density (%)	Manufacturing time (min)	Relative density (%)	Rel. density reduction (%)
Reinforced body centered cube ‡	A	Lattice	A_1	311	27.11	305	24.23	2.88
			A_8	492	27.83	490	26.67	1.16
Dode medium ‡	B	Lattice	B_1	224	13.16	222	12.04	1.12
			B_8	416	13.44	416	13.33	0.11
Dode thick ‡	C	Lattice	C_1	221	25.51	212	21.41	4.10
			C_8	377	26.29	377	25.36	0.93
G-Structure 9 ‡	D	Lattice	D_1	178	23.35	171	19.55	3.80
			D_8	299	23.62	292	20.85	2.77
G-Structure 10 ‡	E	Lattice	E_1	180	30.33	182	26.87	3.47
			E_8	293	31.52	292	26.81	4.71
Octet truss ‡	F	Lattice	F_1	250	30.32	244	27.09	3.23
			F_8	435	30.16	432	28.03	2.13
Rhombic dodecahedron ‡	G	Lattice	G_1	237	30.65	227	25.87	4.79
			G_8	410	31.05	408	29.76	1.28
Truncated octa light ‡	H	Lattice	H_1	233	21.25	226	18.09	3.16
			H_8	373	20.94	373	20.86	0.08
Neovius surface ‡	I	Sk-TPMS	I_1	227	23.75	222	21.71	2.04
			I_8	339	23.63	336	22.23	1.40
Schoen gyroid ‡	J	Sk-TPMS	J_1	197	20.68	192	17.65	3.03
			J_8	289	23.69	280	18.77	4.92
Schwarz diamond ‡	K	Sk-TPMS	K_1	190	24.63	192	22.40	2.23
			K_8	300	24.57	296	23.51	1.06
Cylinder grid ‡	L	Sk-TPMS	L_1	174	26.77	168	21.79	4.98
			L_8	225	27.16	216	21.98	5.17
Schwarz primitive (pinched)‡	M	Sk-TPMS	M_1	185	29.81	179	23.84	5.97
			M_8	241	29.93	234	24.82	5.11
Schwarz primitive ‡	N	Sk-TPMS	N_1	173	18.38	170	14.57	3.80
			N_8	234	18.22	230	15.23	2.99
Body diagonals with nodes ‡	O	Sk-TPMS	O_1	193	46.13	182	37.79	8.34
			O_8	295	47.26	286	39.62	7.65
Gyroid †	P	Sh-TPMS	P_1	29	8.01	–	–	–
			P_8	49	15.99			
Diamond †	Q	Sh-TPMS	Q_1	34	9.75	–	–	–
			Q_8	61	19.45			
Lidinoid †	R	Sh-TPMS	R_1	56	16.29	–	–	–
			R_8	158	30.88			
Split-P †	S	Sh-TPMS	S_1	37	11.74	–	–	–
			S_8	101	21.66			
Schwarz †	T	Sh-TPMS	T_1	25	5.79	–		
			T_8	42	11.78			
Reference	REF	Solid ± 45°	So	66	100.00[a]	–		–

[a] Experimental measurement of Solid ± 45° pattern's density: 1.1457 g/cm^3. Sk-TPMS and Sh-TPMS stand for Skeletal and Shell triply periodic minimal surfaces, respectively.‡ Pattern manufactured with support structures.† Pattern manufactured without support structures.

(Specimen ID_8), respectively. It should be noted that, in some cell designs, the minimum wall thickness achievable by the additive manufacturing equipment limited the range of densities. Thus, the priority has been given to the printability of the samples, not the uniformity of the porosity of the designs.

Specimens were fabricated in a Stratasys Fortus 400mc FFF equipment employing PEI Ultem 9085 (PEI Ultem) material, a high-performance technical polymer with an outstanding strength-to-weight ratio [68]. This professional equipment has a thermal chamber controlled during the printing process. This fact significantly improves the inter-layer adherence between adjacent building layers, thus leading to a higher strength. The oven temperature was set at 195 °C and the model extrusion temperature at 380 °C. All the specimens were manufactured with a layer height of 0.254 mm.

Specimens *A* to *O* were evaluated with two different infill configurations: solid and sparse. Sparse patterns were generated by introducing a separation of 0.25 mm between intra-layer filaments using the raster-to-raster air gap parameter. On the other hand, the constant thickness of Shell-TPMS patterns (*P* to *T*) allows a higher accurate control over the density of the final structure. Thus, aiming to evaluate the potential of FFF technology to produce structures as light as possible, these patterns were printed with solid walls fabricated with a wall thickness of two contours (1.016 mm). Furthermore, a reference solid ± 45° configuration was included in this study. In all cases, two samples of each specimen were manufactured to validate the repeatability of the experimental tests, resulting in 142 manufactured patterns.

The geometric complexity of the studied three-dimensional patterns entailed multiple areas with overhangs, which required support material (polysulfone) for their construction (see Fig. 2). Hence, an optimized procedure employing a recently proposed solvent of 20% v/v aniline in toluene dissolution was used for removing support structures [69,70]. Fig. 1 depicts both unit and eight cells of every considered pattern once the support structures had been chemically removed.

Once all the samples were cleaned, the ratio between each specimen's mass and the Solid ± 45° cube configuration one was calculated (ρ^*/ρ^S) to obtain the relative density measurements. The average result of each pattern and infill configuration is given in Table 1. It should be noted that, since the unit cell in Specimens ID_8 *A* to *O* is equal to the corresponding Specimen ID_1 with a downscaling factor of 50%, the experimental measurement of the relative density leads to equivalent results in all cases. Meanwhile, as pat-

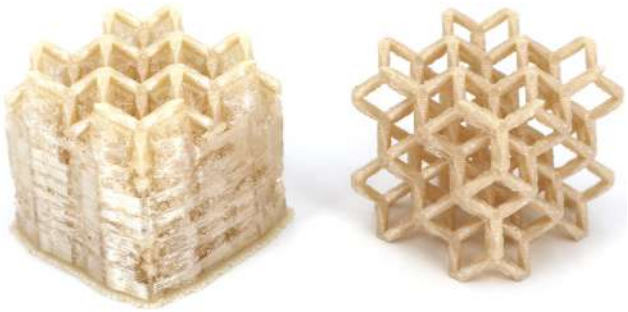

Fig. 2. Appearance of a three-dimensional FFF cellular solid (B_8) with the required support structures for its manufacturing (*left*) and after the cleaning treatment with the 20% v/v aniline in toluene solution (*right*).

terns *P* to *T* were all manufactured with two contours regardless of the unit cell size, the relative density of Specimen ID_8 is double the one corresponding to Specimen ID_1. However, different trends are observed when analyzing the estimated manufacturing time data since Specimens ID_8 required almost twice as much time to build as ID_1 in all cases.

The contribution of the sparse infill to weight reduction depends on the shape of the different building layers that constitute the manufactured part itself. In other words, if any portion of the cross-sectional area of the printed volume is too narrow for fitting both the contours and the infill region with separated rasters, the slicer software automatically sets it as solid. Therefore, weight reduction and printing time savings associated with the use of sparse infill are more evident in those designs where the unit cells are larger. As can be noticed from Table 1 data, sparse infill can suppose up to 8.34% of weight reduction (A_1), whereas just a 0.08% loss is noticeable in other cases (H_8), depending on the pattern's shape. Moreover, the scaling factor used in Specimen ID_8 narrows its cross-section compared to Specimen ID_1. Accordingly, the effectivity of the sparse infill might be limited when used in smaller FFF patterns.

2.2. Compression testing

Printed specimens were tested in compression along the perpendicular axis to the printing plane (see Fig. 3). Tests were conducted using ZwickRoell Z030 30 kN equipment following the ASTM C365 standard [71]. The crosshead rate was set to 3 mm/min. Results from the elastic modulus, the maximum stress prior to first failure (FF), and the corresponding absorbed energy were reported. The specimens' nominal external dimensions (40 × 40 × 40 mm) were employed for effective stress and strain calculations. The experimental elastic moduli were determined from test data between 0.1% and 0.3% of compressive strain using linear regression. Finally, the energy absorption efficiency was calculated as the ratio between the area under the load–displacement curve and the material's volume used for manufacturing each cell pattern.

Each specimen was previously sprayed with a black and white stochastic pattern to determine the full-field deformation of the samples with a 3D Digital Image Correlation (DIC) system. Two Allied Vision GigE MAKO G-507B cameras with APO-Xenoplan 1.4/23–0903 lenses were used to record the tests. A GOM CP20/MV55x44 panel was employed for the setup's calibration. The recorded sequences were post-processed with GOM Correlate Professional software to evaluate the deformation of the samples' surface until failure occurred.

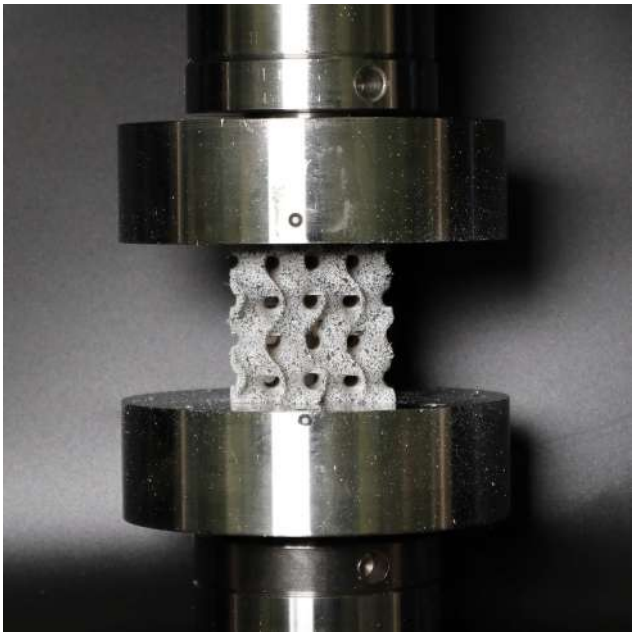

Fig. 3. Experimental setup for compression tests, corresponding to the Specimen P_8.

2.3. Numerical analysis

To assess the elastic performance of each cellular solid numerically, an Ansys FE implicit model was developed[1]. Two approaches were used for numerical analysis: the solid-element model (SE) and the homogenized representative volume element model (H-RVE). In both cases, two rigid bodies were first created on the top and bottom faces of the specimens to represent compression test plates. Displacements and rotations were restricted to fix the bottom plate, while a 0.1 mm displacement was imposed on the upper plate along the loading testing direction. A Normal Stiffness Factor (FKN) was included in the contacts' definition to reproduce the phenomenon of elastic asymmetry [72]. This factor was calibrated with the experimental data from Solid ± 45° infill samples, obtaining a FKN factor of 0.050. Next, frictional contacts with asymmetric behavior were defined between the cellular pattern and the plates, with a friction coefficient of 0.42. In addition, augmented Lagrange formulation with a penetration tolerance of 0.1 mm was activated, and ramped effects were permitted. The reaction force was finally calculated on the bottom surface to determine the stiffness of the cellular pattern. In every case, both displacement and load values were stored for every intermediate step of the simulation until the convergence of the model was reached. Finally, the numerical elastic moduli were again determined using linear regression and the nominal external dimensions of the sample.

For the SE approach, the CAD geometry of the cellular pattern was imported and discretized with a body mesh method, employing higher-order 20-node SOLID186 elements of 0.50 mm. The mechanical properties of the PEI Ultem 3D printed material were adopted from a previous comprehensive study [68], and are summarized in Table 2.

The second approach aimed to validate a more computationally efficient strategy for numerical analysis through a homogenized RVE model [73,74]. First, each three-dimensional pattern's unit cell was numerically homogenized using Ansys Material Designer with periodic boundary conditions, obtaining the performance compli-

[1] FE models were solved using the following hardware: AMD Ryzen Threadripper 2920X 12-Core Processor and RAM Memory 64 Gb DDR4 2133 MHz; License Solver: 4 Physical CPU Cores Used

Table 2
PEI Ultem 9085 Quasi-Isotropic elastic properties and stress limits used in the solid-element model (SE) [57].

Orthotropic Elasticity		
Young's Modulus *x*-direction (MPa)	E_x^s	2121
Young's Modulus *y*-direction (MPa)	E_y^s	2121
Young's Modulus *z*-direction (MPa)	E_z^s	2126
Poisson's Ratio *xy*	ν_{xy}^s	0.344
Poisson's Ratio *yz*	ν_{yz}^s	0.392
Poisson's Ratio *xz*	ν_{xz}^s	0.392
Shear Modulus *xy* (MPa)	Gs_{xy}	630
Shear Modulus *yz* (MPa)	G_{yz}^s	741
Shear Modulus *xz* (MPa)	G_{xz}^s	741
Orthotropic Stress Limits		
Tensile *x*-direction (MPa)	$\sigma_{T,x}^s$	24.45
Tensile *y*-direction (MPa)	$\sigma_{T,y}^s$	24.45
Tensile *z*-direction (MPa)	$\sigma_{T,z}^s$	24.45
Compressive *x*-direction (MPa)	$\sigma_{C,x}^s$	−24.45
Compressive *y*-direction (MPa)	$\sigma_{C,y}^s$	−24.45
Compressive *z*-direction (MPa)	$\sigma_{C,z}^s$	−24.45
Shear *xy* (MPa)	τ_{xy}^s	25.72
Shear *yz* (MPa)	τ_{yz}^s	25.93
Shear *xz* (MPa)	τ_{xz}^s	25.93

ance matrix of each cellular solid. Next, the cubic nominal volume was also modeled with a body mesh method, employing the previously mentioned element type and size. Finally, the homogenized performance tensors were introduced in the FE model, and the effective elastic properties were applied to the cubic RVE for the numerical analysis.

2.4. Degree of anisotropy

The degree of anisotropy quantifies the uniformity of the mechanical performance of a material in all the orientations. Three approaches have been adopted for comparative purposes to estimate the degree of anisotropy: the Zener index [75], the Universal anisotropy index [76], and the volume-based index proposed in this work.

The Zener anisotropy index *A*, which was initially introduced to measure the anisotropy of cubic crystals, can be directly computed from the coefficients of their stiffness tensor ($\boldsymbol{C}$) as:

$$A = \frac{2C_{44}}{C_{11} - C_{12}} \tag{1}$$

where:

$$\boldsymbol{C} = \begin{bmatrix} C_{11} & C_{12} & C_{13} & 0 & 0 & 0 \\ & C_{22} & C_{23} & 0 & 0 & 0 \\ & & C_{33} & 0 & 0 & 0 \\ & & & C_{44} & 0 & 0 \\ & Sym. & & & C_{55} & 0 \\ & & & & & C_{66} \end{bmatrix}$$

Physically, C_{44} represents the stiffness with respect to a shearing stress applied across the (1,0,0) plane in the [0,1,0] direction. Similarly, $(C_{11} - C_{12})/2$ represents the resistance to shear deformation by shear stress applied across the (1,1,0) plane in the [1,-1,0] direction (see Fig. 4). This calculation results in *A* values that range from 0 to ∞, depending on the coefficients of the stiffness tensor ($\boldsymbol{C}$), becoming $A = 1$ for a locally isotropic solid since the above shear resistances would be equal. Moreover, some authors prefer to quantify the anisotropy as A^{-1} instead of *A*. Thus, and despite the fact the Zener index has been recently applied in the field of

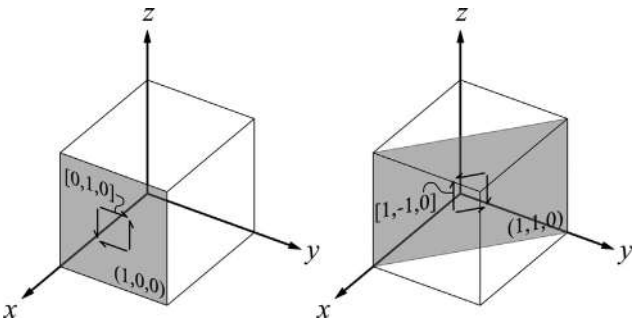

Fig. 4. Diagrams of the shear stresses corresponding to C_{44} (*left*) and $(C_{11} - C_{12})/2$ (*right*) that are evaluated for the calculation of the Zener anisotropy index (*A*).

FFF cellular solids [6,77], other authors previously concluded that *A* is restricted to cubic crystals and lacks universality [76], and the Universal anisotropy index A^U was proposed:

$$A^U = \frac{6}{5}\left(\sqrt{A} - \frac{1}{\sqrt{A}}\right)^2 \tag{2}$$

A^U is a single-valued measure whose null value stands for isotropic behavior. However, *A* and A^U assume that $C_{11} = C_{22} = C_{33}$, $C_{12} = C_{13} = C_{23}$, and $C_{44} = C_{55} = C_{66}$ in the stiffness tensor (C). Thus, although three-dimensional cellular solids usually display an apparent symmetry in the 3D space, these assumptions may be questioned regarding the inherent anisotropy of AM-fabricated patterns which has been widely reported, especially in extruded-like designs [78,79]. Therefore, a more general and robust method to quantify the anisotropy of additively manufactured cellular solids should contribute to the development of functional designs that can be implemented in fully end-parts.

Accordingly, a novel degree of anisotropy index A^V is proposed in this work based on the ratio between the volumes of the graphical representation of the whole stiffness tensor and the corresponding isotropy circumscribed sphere (see Fig. 5). This index can only handle values from 0 to 1, being $A^V = 1$ perfectly isotropic.

2.5. Flexural validation test

Finally, to validate and compare both numerical approaches, the performance of a two-dimensional pattern (Hexachiral), and a three-dimensional Shell-TPMS design (Q) were experimentally and numerically evaluated under a centered 3-point bending load case. Tests were conducted using ZwickRoell Z030 30 kN equipment, following the ASTM D790 standard [80]. The crosshead rate was set to 3 mm/min. The sample's nominal external dimensions ($20 \times 20 \times 200$ mm) were considered to calculate stress and strain data. In both cases, two repetitions were tested to validate the experimental results.

3. Results and discussion

3.1. Compressive performance

Fig. 6 depicts representative stress–strain curves obtained thought the experimental compression tests of the 3D printed specimens. The data presented corresponds to the unit (ID_1) and the eight-cell (ID_8) samples of lattice (E), Skeletal-TPMS (I), and Shell-TPMS (Q) patterns with both solid and sparse infill configurations.

As can be seen, depicted results are experimental evidence of the pattern design's influence on mechanical performance. Moreover, it should be noted that each cellular solid exhibits a similar

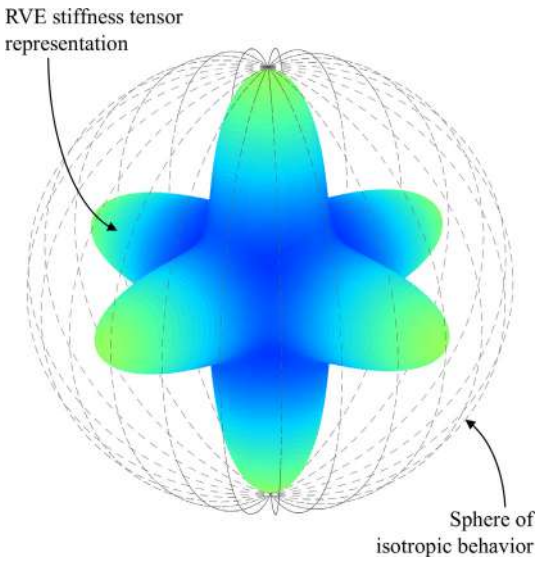

Fig. 5. Volumetric representation of the RVE stiffness tensor corresponding to the family M, and the isotropic circumscribed sphere. The ratio of these two volumes is the A^V anisotropy index.

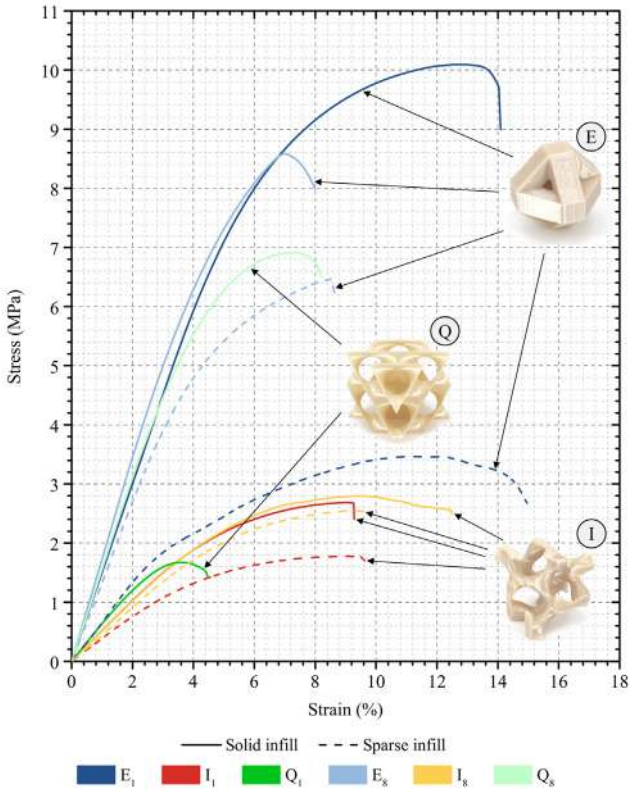

Fig. 6. Stress–strain representative curves obtained from the experimental compression tests performed on the cellular solids patterns.

stiffness regardless of the unit cell's dimensions when its geometry is perfectly scaled (see solid examples *E* and *I*). On the contrary, in those specimens where wall thickness was kept fixed at two contours (see example *Q*), the elastic modulus of Specimen ID_8 approximately doubles the corresponding unit-cell sample, as the first one is denser and exhibits a larger effective area. Furthermore, the stress–strain curves confirm that the bigger the unit cell is, the higher the yield and maximum stress the structure reaches. Hence, although scaling the cell size may not influence the stiffness property, the FFF toolpaths that constitute the resulting part must be considered. Thus, using tiny unit cells in this AM technology can lead to the appearance of multiple infill voids that might become stress concentrators as the 3D printing equipment resolution is still limited.

Major variations arise when comparing the performance of the solid and the sparse infill samples. In particular, when sparse infill is used in patterns formed by larger unit cells, the infill setting has a more significant impact on the structures' mechanical behavior, as expected. This point is related to the fact that having too narrow areas in the cross-section disables sparse infill in favor of solid infill in the affected areas. Accordingly, as pointed out when the relative density data was presented (see Section 2.1), many of the Specimen ID_8 samples are practically solid despite using the sparse infill setting in the slicer software. This fact is noticeable on stress–strain curves from samples *E* and *I*. As shown, sparse infill in Specimens ID_1, which have thicker unit cells than Specimens ID_8, leads to a more significant decrease in the elastic modulus, the maximum strength, and the total absorbed energy before the first failure (FF) occurs.

Fig. 7 depicts the results of the experimental compression performance of the three-dimensional cellular solids in terms of the relative density (*left*) and the time required for the fabrication (*right*). Experimental data of PEI Ultem two-dimensional patterns from a previous research [54], which were fabricated and tested employing the same methodology described in the present study, is overlapped for comparison.

The mechanical performance of families *E*, *M*, and *Q* is highlighted in each plot as representative patterns of lattice, Skeletal-TPMS, and Shell-TPMS typologies, respectively. Depicted results allow several conclusions to be drawn. On the one hand, cell geometry design leads to different dimensions and orientations of the resistant sections. This fact explains the differences in the results on the vertical axis within specimens of similar relative density in the charts in the left column. On the other hand, the elastic modulus, the compression strength at failure, and the energy absorption efficiency are significantly superior to that obtained by two-dimensional patterns in the in-plane cell's orientation for an equivalent relative density. This difference is mainly attributed to the material's distribution in their cross-section and the presence of manufacturing defects. That is, as the two-dimensional designs have mainly closed cells and were printed with the thinnest wall-thickness possible of one single contour, the filament paths create numerous discontinuities (intra-layer defects), resulting in manufacturing imperfections that compromise the load-bearing capacity and energy absorption efficiency. In contrast, the three-dimensional patterns show a wide range of wall thicknesses depending on the chosen cell design, which are manufactured with multiple filament contours. Hence, the material's deposition is concentrated in stronger sections while keeping the same relative density and employing continuous filament paths, which favors the reduction of defects between joints and significantly improves the load capacity and energy absorption efficiency. For these reasons, deposition imperfections become more critical for the mechanical performance of 2D patterns than in 3D designs since an inaccurate union of the cells (intra-layer defects) of the former results in an earlier breakage. Therefore, as the absorbed energy efficiency results have been reported up to the first failure of the specimens, thin-walled two-dimensional morphologies are less efficient in absorbing energy than three-dimensional alternatives, despite exhibiting equivalent relative densities. However, none of the three-dimensional specimens displayed a stiffness higher than the one achieved with two-dimensional patterns' in the out-of-plane arrangement (perpendicular to the printing plane). This fact is explained because 3D patterns mainly work under bending

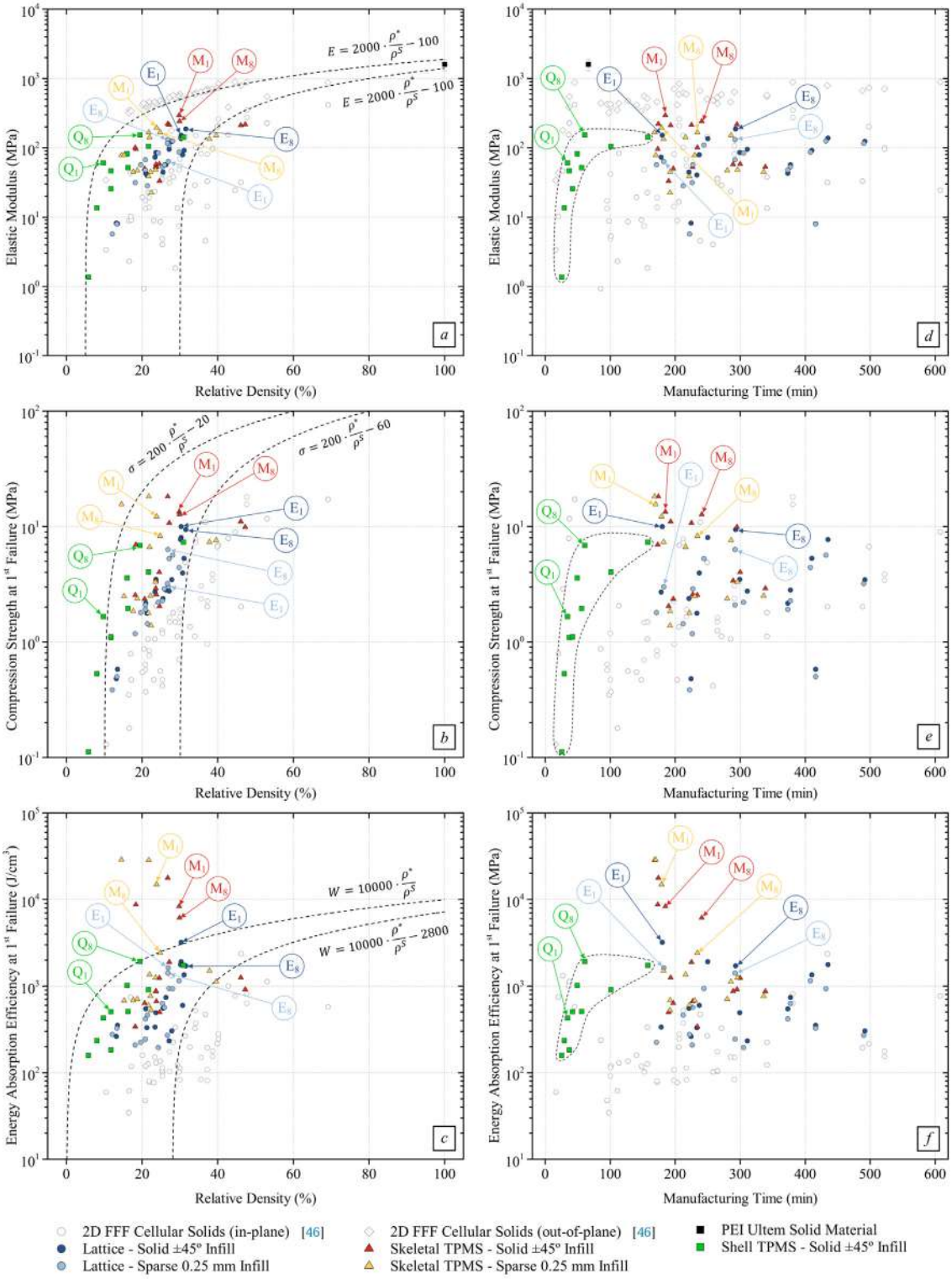

Fig. 7. Experimental results of the elastic modulus (*a, d*), compression strength (*b, e*) and energy absorption efficiency (*c, f*) in terms of relative density and manufacturing time for each cellular solids pattern.

stress, thus showing a more flexible performance, while compression stresses in 2D patterns produce the buckling of the cell walls.

Despite dispersion, scatter plots *a*, *b*, and *c* in Fig. 7 show a trend between mechanical performance and the relative density of the samples, as expected. Focusing on maximizing the mechanical properties (*y*-axis) and minimizing the weight of the structures (*x*-axis), an in-depth analysis of these charts provides relevant information to determine which cell typologies stand out. Accordingly, experimental evidence states that the Shell-TPMS designs proved to be the most efficient ones, followed by the Skeletal-TPMS and, finally, the lattice configurations. Furthermore, paying attention to the fabrication process, the scatter plots

d, *e*, and *f* show that the Shell-TPMS designs require less than half the fabrication time as the other cell patterns. This fact is explained by the need to use support structures to fabricate the other patterns, which involve a time-consuming material deposition sequence.

Accordingly, the Shell-TPMS designs allow the fabrication without support structures, which means that the FFF equipment does not need to perform the material change sequence, and a considerable amount of time is saved by avoiding purging steps. However, despite requiring purging steps, Skeletal-TPMS and lattice designs still can compete in manufacturing time against two-dimensional patterns. Fig. 7 highlights that three-dimensional designs offer better mechanical performance than two-dimensional patterns employing the same amount of time for construction.

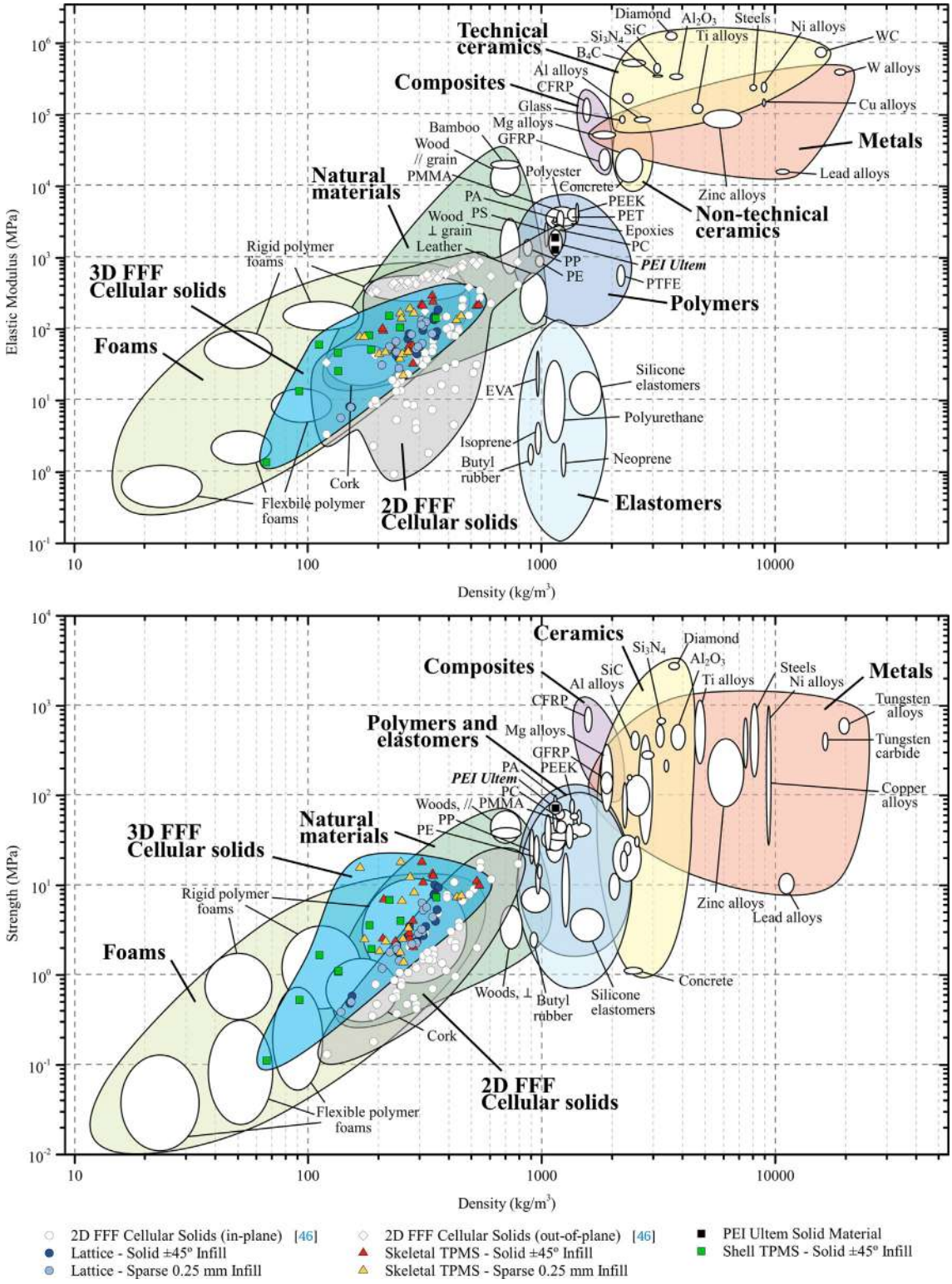

Fig. 8. Comparison of the experimental performance of the 2D [57] and 3D FFF cellular solids with materials database adapted from CES EduPack 2019, ANSYS Granta © 2020 Granta Design, with permission.

3.2. Comparative performance

Experimental results have been represented in Fig. 8 to compare the structural performance of the FFF cellular solids patterns in terms of stiffness, compression strength, and density. In addition, results from available PEI Ultem two-dimensional cellular solids are included in a gray shaded area, as well as the mechanical properties of other materials from the Ansys GRANTA EduPack database, for comparison. As shown, the performance of cellular solids is contained in the range of foams and natural materials. However, the three-dimensional designs cover a different region from the two-dimensional ones.

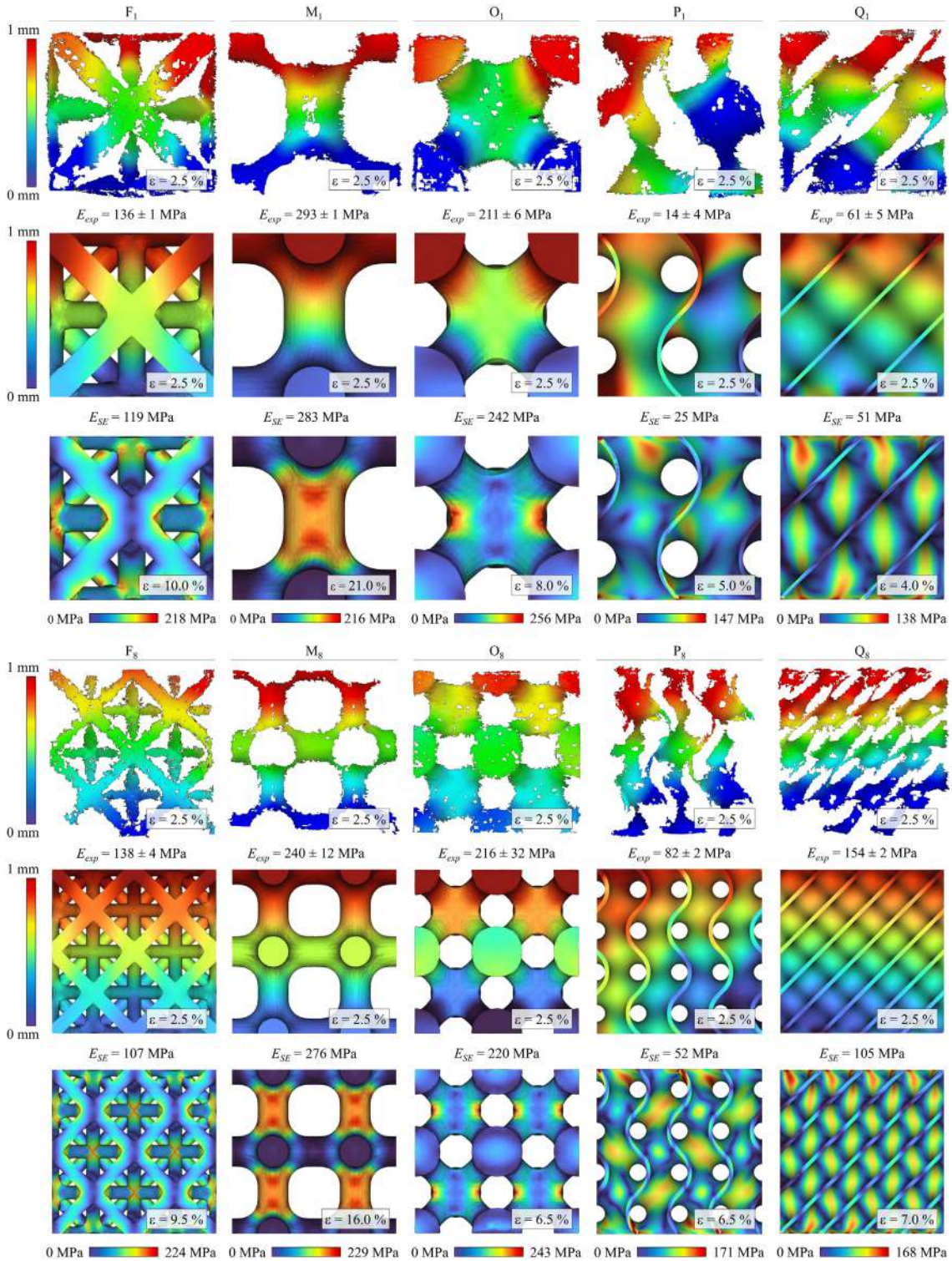

Fig. 9. Comparison results of the numerical solid-element model and experimental data of ten representative cellular solids tested under compression load. The first and fourth rows correspond to the experimental displacement field obtained via digital image correlation. The second and fifth rows are the analogous numerical displacement fields, while the third and sixth rows display the numerical Von Mises stress before the specimen's failure.

Both charts in Fig. 8 contain black square dots representing the reference PEI Ultem material properties processed in FFF (Solid ± 45° with 100% infill density). Focusing on the *top* chart, cellular patterns display lower elastic modulus than the solid reference, attending to the fact that less material is used. On the other hand, regarding the wide spectrum of the achieved results, the cell's design plays an important role on the mechanical properties and density of the pattern, as was intended to demonstrate. As previously noticed in Fig. 7, when samples of similar densities are compared, three-dimensional patterns exhibit intermediate stiffnesses between two-dimensional designs' in-plane and out-of-plane behaviors. In particular, while their elastic moduli are not too far from the results achieved with the optimum out-of-plane orientation of two-dimensional designs, the in-plane performance is improved by up to two orders of magnitude. Therefore, three-dimensional designs tend to reduce the orthotropy of the cellular solid, as will be further discussed in Section 3.4.

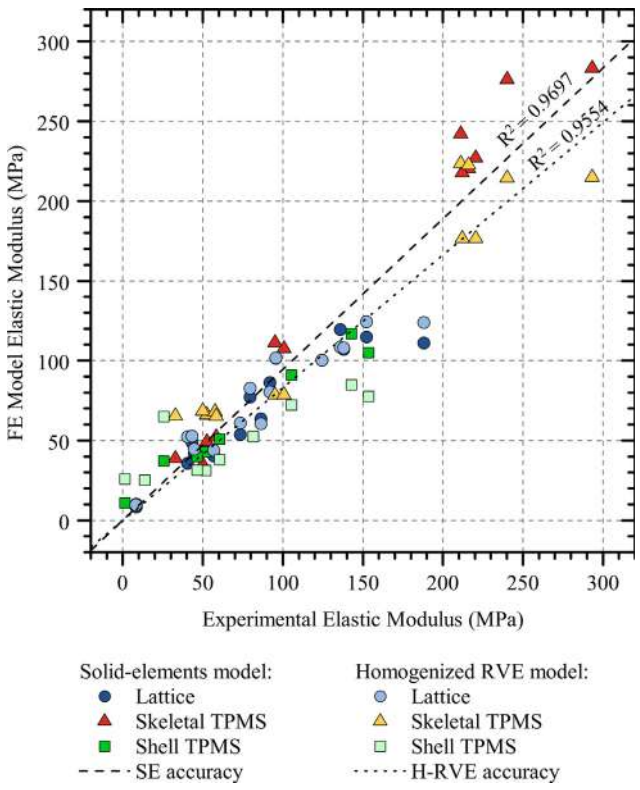

Fig. 10. Comparison of the accuracy of the solid-element and homogenized RVE numerical models in constrast to experimental data.

The *bottom* chart in Fig. 8 allows the comparison of the different materials in terms of compression strength and density. It should be noted that out-of-plane compression strength results from two-dimensional cellular solids are not reported in the literature, hence not included. Overall, when similar densities are examined, depicted results state that the compression strength of the three-dimensional designs is significantly higher than the in-plane strength of the two-dimensional cell designs. This experimental evidence is explained by the fact that 3D geometries behave stretch-dominated while 2D behave bending-dominated. Moreover, inherent manufacturing imperfections extensively reported in [54] create discontinuities in the cell-wall connections, which proved to have dramatic effects on the performance of two-dimensional cellular solids. In contrast, three-dimensional cell patterns proved to be less prone to manufacturing defects.

3.3. Numerical analysis

Firstly, the numerical results obtained with the SE approach are discussed. This model offers a shorter setup and accounts for geometric details from the cellular solids while considering edge

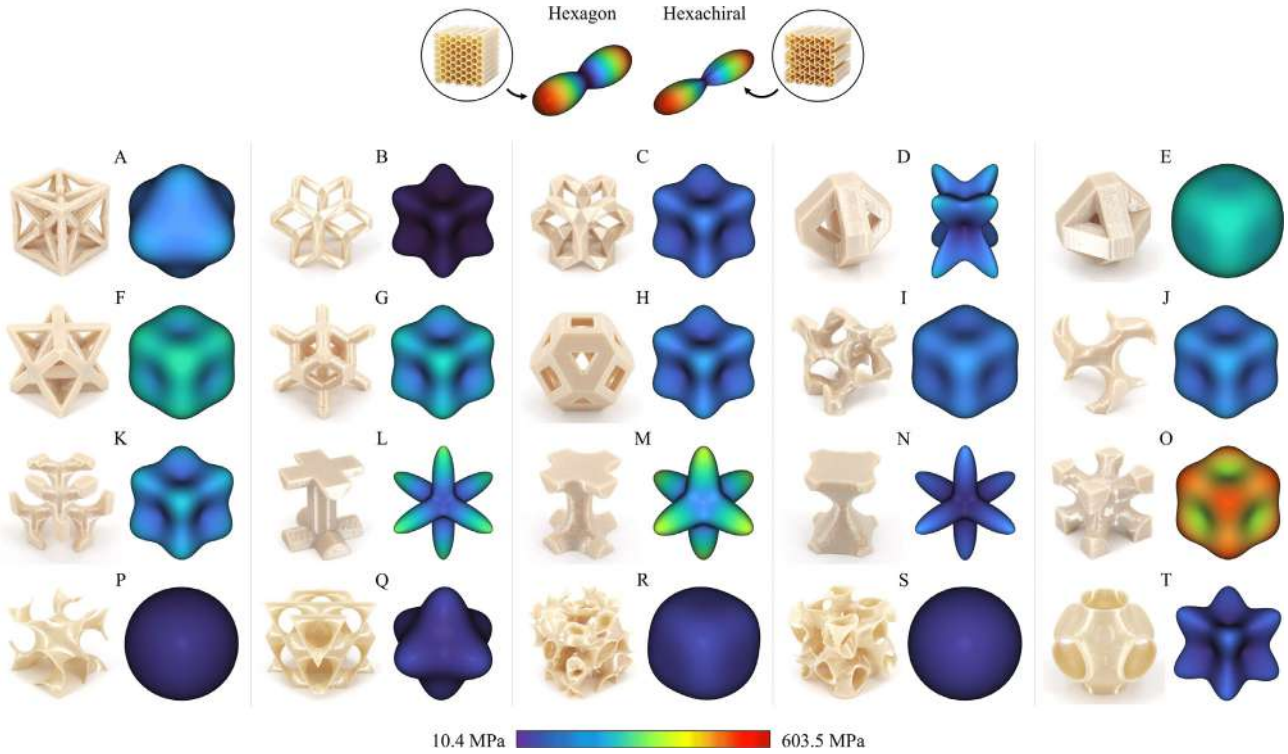

Fig. 11. Homogenized stiffness tensor representations for each of the studied patterns (see 6). Two-dimensional cellular designs (Hexagonal and Hexachiral) are included for comparison.

effects. Nevertheless, it presents a major drawback of being very computationally expensive. Fig. 9 compares the numerical and experimental data of ten representative cellular solids tested under compression load. The first and fourth rows correspond to the experimental displacement field obtained via digital image correlation (DIC) for a 1 mm (2.5% of strain) compression displacement along the perpendicular axis to the printing plane. Deficiencies observed in the displacement field are due to limitations in recognizing the stochastic pattern sprayed on the surface of the samples, particularly on regions not visible to one of the cameras (see specimens *P* and *Q*). The second and fifth rows are the analogous numerical displacement fields, while the third and sixth rows display the numerical Von Mises stress before the specimen's failure. In addition, the experimental and numerical stiffness moduli are indicated below each image, corresponding to the results obtained from compression tests and employing the SE model, respectively. In general, the numerical results agree with experimental values as well as with reference material data [81], thus validating the numerical model.

Von Mises stresses show different trends between cellular patterns, particularly on Shell-TPMS designs (see specimens *P* and *Q*). Overall, the identified areas of stress concentration match the experimental failure regions of the cellular solids. Note that walls in Shell-TPMS designs are not self-intersecting surfaces, hence avoiding joints and discontinuities in filament deposition. This fact favors the stress distribution and improves the mechanical performance of the cellular structure, thus confirming the experimental evidence.

Secondly, a much more computationally efficient alternative to simulate cellular structures is implementing the H-RVE model. Specifically, the effective and homogenized elastic properties of a RVE are used to define the behavior of the cellular structure which, in this case, is simplified into a completely solid model that covers the cubic envelope of the sample. Thus, it is a remarkably robust method to simulate cellular solids regardless of their geometrical complexity, density, and cell dimensions, reducing the meshing process complexity considerably.

However, implementing the H-RVE approach for simulating periodic structures has certain drawbacks that must also be considered. On the one hand, it is only suitable for uniform repetitive geometries, as the effective RVE properties are supposed to be constant throughout the volume. On the other hand, this approach requires computing more steps since a homogenization of the unit cell has to be performed before addressing the whole design. Moreover, this numerical analysis tends to be less accurate than the SE method because neither edge effects nor stress concentrations are considered due to the simplification of the model.

The accuracy of both numerical methods is presented in Fig. 10, where the values of the estimated elastic moduli of each cellular solid are compared with the experimentally determined ones. A regression line is fitted to each numerical approach, and the coefficient R^2 is given to quantify the degree of correlation. As can be

Table 3
Results of three indices to quantify the degree of anisotropy of each cell pattern.

Specimen ID	A^V	A[6,75,77]	A^U[79]	Relative density (%)	Elastic modulus (MPa)	Compression strength at FF (MPa)	Energy absoroption efficiency at FF (J/cm^3)
S_8	0.997	0.999	0.000	21.7	105 ± 0	4 ± 0.0	908 ± 8
S_1	0.966	1.030	0.001	11.7	47 ± 3	1.1 ± 0.0	184 ± 5
P_1	0.950	1.051	0.003	8.0	14 ± 4	0.5 ± 0.1	235 ± 15
P_8	0.911	1.087	0.008	16.0	82 ± 2	3.6 ± 0.1	1019 ± 60
R_8	0.876	1.141	0.021	30.9	143 ± 1	7.3 ± 0.1	1733 ± 28
E_8	0.829	1.204	0.041	31.5	188 ± 21	9.4 ± 1.2	1722 ± 598
E_1	0.827	1.207	0.042	30.3	152 ± 3	10 ± 0.1	3209 ± 55
R_1	0.820	1.220	0.047	16.3	52 ± 2	2 ± 0.1	511 ± 3
F_1	0.632	1.641	0.301	30.3	136 ± 1	8 ± 0.1	1924 ± 77
F_8	0.631	1.633	0.294	30.2	138 ± 4	7.7 ± 0.2	1775 ± 67
A_1	0.611	0.709	0.144	27.1	96 ± 12	2.8 ± 0.1	234 ± 34
A_8	0.610	0.709	0.143	27.8	124 ± 2	3.5 ± 0.2	305 ± 34
I_1	0.606	1.653	0.310	23.7	52 ± 1	2.6 ± 0.2	664 ± 103
I_8	0.605	1.639	0.299	23.6	53 ± 1	2.9 ± 0.2	863 ± 28
O_1	0.590	1.843	0.463	46.1	211 ± 6	11 ± 0.6	1252 ± 182
O_8	0.589	1.852	0.470	47.3	216 ± 32	9.9 ± 1.6	914 ± 163
J_1	0.585	1.812	0.437	20.7	50 ± 2	2.4 ± 0.1	635 ± 143
J_8	0.582	1.791	0.419	23.7	58 ± 0	3.4 ± 0.3	873 ± 95
Q_8	0.570	0.682	0.178	19.4	154 ± 2	6.9 ± 0.1	1927 ± 12
G_1	0.548	2.070	0.664	30.7	80 ± 4	4 ± 0.3	601 ± 134
G_8	0.547	2.101	0.693	31.0	92 ± 2	5.3 ± 0.2	1350 ± 26
H_8	0.524	2.419	0.998	25.5	43 ± 1	2.2 ± 0.0	545 ± 103
H_1	0.523	2.411	0.991	20.9	40 ± 1	1.8 ± 0.0	331 ± 5
C_1	0.523	2.294	0.876	21.3	45 ± 0	2.4 ± 0.1	554 ± 18
C_8	0.521	2.347	0.927	26.3	57 ± 0	2.8 ± 0.0	741 ± 31
K_8	0.520	2.313	0.894	24.6	58 ± 0	4 ± 0.0	1243 ± 34
K_1	0.519	2.327	0.908	24.6	33 ± 3	2 ± 0.4	496 ± 164
Q_1	0.508	0.590	0.342	9.8	61 ± 5	1.7 ± 0.0	429 ± 2
T_8	0.503	2.611	1.193	11.8	26 ± 0	1.1 ± 0.0	507 ± 28
B_1	0.494	2.656	1.239	13.2	8 ± 0	0.5 ± 0.0	263 ± 5
B_8	0.491	2.597	1.179	13.4	8 ± 0	0.6 ± 0.0	352 ± 5
T_1	0.473	3.271	1.892	5.8	1 ± 0	0.1 ± 0.0	158 ± 46
M_1	0.392	0.290	2.091	29.8	293 ± 1	13.3 ± 1.5	8302 ± 1451
M_8	0.391	0.289	2.103	29.9	240 ± 12	12.7 ± 0.4	6125 ± 257
D_8	0.385	0.126	7.285	18.2	86 ± 1	3.5 ± 0.2	493 ± 94
D_1	0.365	0.124	7.415	18.4	73 ± 4	2.7 ± 0.1	337 ± 13
N_1	0.365	0.184	4.351	26.8	95 ± 3	6.9 ± 0.3	8710 ± 1477
N_8	0.364	0.184	4.351	27.2	101 ± 3	2.5 ± 0.0	339 ± 17
L_1	0.360	0.181	4.443	23.4	221 ± 19	18.1 ± 0.0	17764 ± 690
L_8	0.360	0.182	4.413	23.6	212 ± 3	10.7 ± 0.1	1887 ± 51

seen, both models tend to underpredict the cellular stiffness, but the best fit corresponds to the SE model, even though the H-RVE model leads to huge computational time savings.

3.4. Degree of anisotropy

The geometric complexity of cell pattern designs, which strongly influences mechanical performance, is linked to the degree of anisotropy. To better illustrate the concept of degree of anisotropy, Fig. 11 depicts the stiffness tensor representations for each of the studied patterns. This graphical depiction allows visualization of the effective elastic modulus in each direction of the space. Thus, the more spherical this graphic is, the more isotropic the cellular pattern performs. These plots are obtained by rotating the homogenized stiffness tensor about the three global coordinate axes, as detailed in Appendix B. The tensor representations of two two-dimensional cellular designs (Hexagonal and Hexachiral) have also been included for comparison.

A first qualitative analysis of these results confirms the influence of the patterns' geometry on the degree of anisotropy. Firstly, there is a noticeable difference between the results of two and three-dimensional cellular solids. The extruded-like geometry of the firsts gives them a high out-of-plane stiffness, while the rigidity in the other planes is compromised. The three-dimensional designs provide balanced stiffness in orthogonal directions, making the graphical representation of the tensor less direction-dependent. Secondly, the arrangement and orientation of the cells, together with the density of the pattern, directly affect the dimensions and orientations of the resistant sections, thus conditioning the performance, as previously verified by experimental tests.

Three approaches were used for comparative purposes to quantify the degree of anisotropy: the Zener index A, the Universal anisotropy index A^U, and a novel proposed volume-based index A^V. Results of three indices are collected in Table 3. According to the A^V index, specimen IDs are sorted from the highest to the lowest degree of isotropy achieved. In addition, results of the mechanical behavior characterization have also been included. As observed, the cell patterns *S*, *P*, *R*, and *E* present the highest isotropic behavior, agreeing with the results depicted in Fig. 11. As can be seen, the reported values highlight the instability of the other indices, A^U and particularly A, to sort the different designs according to their anisotropy degree accurately. In detail, the three indices coincide in the first few patterns, but from the ninth row onwards, the degree of anisotropy obtained by the different indicators diverges significantly. It is explained by the fact that the A^V index is determined employing the whole stiffness tensor, considering the inherent anisotropy of the AM patterns, in contrast to the A^U and A indices.

Fig. 12 depicts the experimental results of the stiffness and specific strength against the degree of anisotropy index A^V. Note that axes are presented in logarithmic scale, and comparison lines are included based on the design criteria E/A^V, $E^{-1/2}/A^V$, and $E^{-1/3}/A^V$. As can be noticed, the three inspected typologies of solid cellular families occupy distinguishable regions in both graphs. The main differences are observed between skeletal and Shell-TMPS patterns. Overall, the former exhibits a superior mechanical performance, while the latter shows higher isotropy. Meanwhile, lattice designs are mainly located in the central area of both plots. In addition, the results also allow determining the effect of cell size. As shown, some geometries have the same anisotropy index, regardless of cell size. However, it does not happen in those specimens where wall thickness was kept fixed at two contours (patterns *P* to *T*), where the relative density of Specimen ID_8 is double the one corresponding to ID_1, and the elastic modulus of Specimen ID_8 has approximately doubled the corresponding unit cell sample

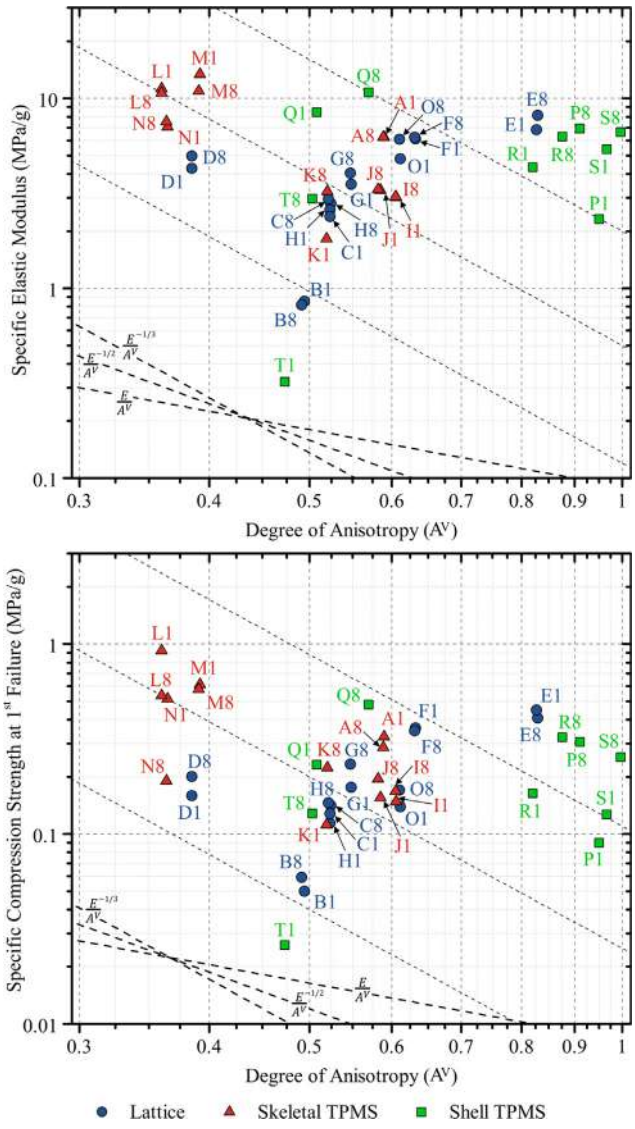

Fig. 12. Experimental results of the specific elastic modulus and compression strength against the degree of anisotropy index A^V of each cellular pattern (see Fig. 1 and Table 1).

(see example Q) due to the fact that the first one is denser, hence exhibiting a larger effective area. Finally, this comparison highlights the mechanical behavior of the Shell-TMPS type patterns, which is added to the advantages in manufacturing time presented above.

3.5. Validation test

Finally, to validate and compare both numerical approaches, the behaviors of a two-dimensional pattern (Hexachiral) and a three-dimensional Shell-TPMS design (Q) were experimentally and numerically evaluated under a centered 3-point bending load case.

The numerical and experimental results of both solid cellular patterns are represented in Fig. 13. The left-hand column corresponds to the two-dimensional Hexachiral pattern and the right-hand column to the three-dimensional Shell-TPMS pattern. The depicted results of each pattern were evaluated when failure occurred. The provided numerical plots show the total displacement and the Von Mises stress obtained results for both patterns employing the SE and the H-RVE approaches, respectively. In addi-

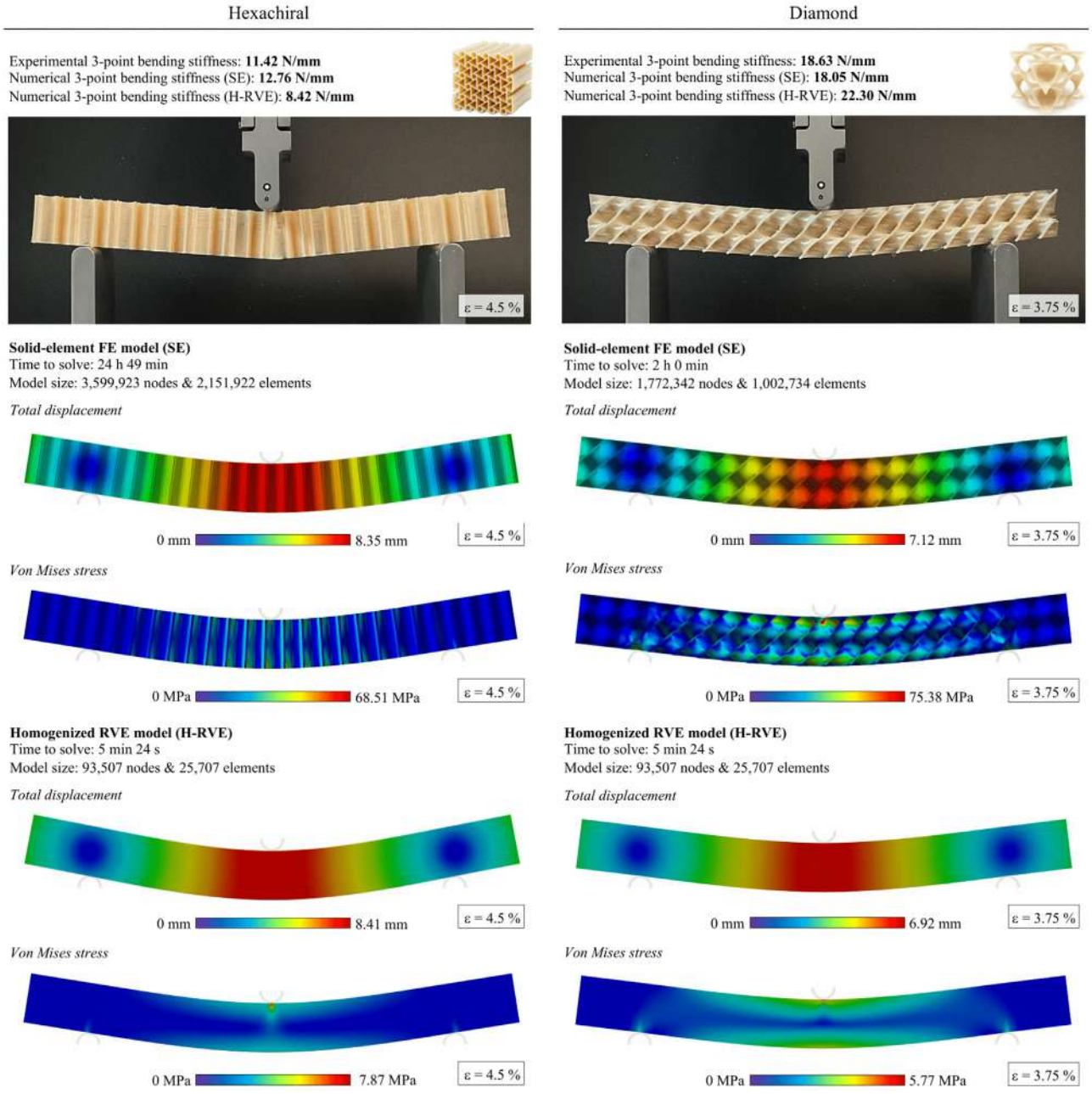

Fig. 13. Validation results of solid-element and homogenized RVE numerical models for Hexachical (*left*) and Diamond (*right*) cellular patterns.

tion, the experimental stiffness of each pattern is included together with the values calculated using both FE methods. Lastly, other model details including the computational time and size are provided.

The numerical stiffness values agree with the experimental result for both types of cellular solids. The higher divergence is observed in the H-RVE approach, which is attributed to the simplification of the homogenized model. Regarding this model, the displacement results from the Hexachiral pattern analysis are satisfactory. However, the bending-torsion coupling effect observed in the Diamond pattern is not identified. Note the slightly different stress field on the surrounding area of supports. Similarly, as displayed on the Von Mises stress plots, the stress concentrators are not captured in the homogenized model. Therefore, only effective stress values can be determined if this approach is implemented. Note the difference between the maximum Von Mises stresses results obtained with the H-RVE and SE methods. Nevertheless, despite these points, the accuracy of the numerical results confirms the capability of both approaches to reproduce the elastic behavior of cellular solids with adequate confidence.

4. Conclusions

This work presents comprehensive research on the mechanical performance of additively manufactured three-dimensional lightweight cellular solids, including open-cell and closed-cell patterns with different cell sizes and infill densities. The paper provides experimental evidence on the differences over two-dimensional designs in terms of stiffness and strength while attending to manufacturing aspects such as printing time, proving that the elastic modulus, the compression strength, and the energy absorption efficiency are significantly superior to that obtained by two-dimensional patterns in the in-plane cell's orientation for an equiv-

alent relative density. The control of the examined engineering parameters allows producing lightweight structures with an extensive spectrum of specific stiffness and strength, starting from the intrinsic properties of a single material. Experimental evidence states that the Shell-TPMS designs proved to be the most efficient cellular pattern, followed by the Skeletal-TPMS and, finally, the lattice configurations. Regarding the fabrication process, results showed that the Shell-TPMS designs require less than half the fabrication time of the other cell patterns.

Two validated strategies for simulating the elastic behavior of cellular solids have also been presented, comparing their accuracy and computational requirements. In short, the homogenized representative volume element approach (H-RVE) has computational advantages (90% less time) but does not allow the simulation of local effects on the cell walls. In contrast, the solid-element approach (SE) can simulate the elastic behavior satisfactorily, including local effects, but at a higher computational cost. In particular, this approach successfully identified the stress concentration regions of the lattice and Skeletal-TPMS patterns where experimental failure occured. In addition, the obtained results proved that the morphology of Shell-TPMS designs favors a more homogeneous stress distribution, which improves the mechanical performance of the cellular structure.

Moreover, the novel method for quantifying the isotropy of the additively manufactured cellular solids presented, based on the graphical representation of the homogenized stiffness tensor, allows comparing the degree of anisotropy of the complex structures in a more robust way, regarding important aspects such as the inherent anisotropy of additively manufactured components.

Lastly, the obtained results highlight how pattern design impacts the cellular solids' density and mechanical behavior. Thus, an accurate adjustment of the unit cell shape can lead to structures with equivalent densities but with very contrasting performances. This fact is illustrated by the significant differences that emerge between the performance that can be achieved with two-dimensional and three-dimensional cellular solids. In particular, the geometric homogeneity in the 3D space of many considered patterns results in a higher degree of isotropy in contrast to the one that is exhibited by the extruded-like designs. Overall, the gathered experimental and numerical data states the advances in mechanical performance and isotropy that implementing three-dimensional designs brings, compared to the more classical two-dimensional patterns.

Data availability

The raw data required to reproduce these findings are available to download from Mendeley Data, https://doi.org/10.17632/zhygf2vdsr.1, including the original STL files that were used to fabricate the samples for this research, mechanical testing raw data, and HD images. Kindly cite this article and the dataset if utilizing or modifying the data in your work.

Declaration of Competing Interest

The authors declare that they have no known competing financial interests or personal relationships that could have appeared to influence the work reported in this paper.

Acknowledgments

This work has been supported by the Ministry of Science, Innovation and Universities through the projects New Developments in Lightweight Composite Sandwich Panels with 3D Printed Cores (3DPC) - RTI2018-099754-A-I00 and Development of Gyroid-Type Cellular Metallic Microstructures by FFF to Optimize Structural Components with High Added-Value (GRIM) - PID2021-123876OB-I00. The authors would like to acknowledge their gratitude to A. Chueca, H. García, S. Oudas, and R. Estrada for the assistance during this research and constructive suggestions.

Appendix A. Generation methods of TPMS cellular solids

All Skeletal-TPMS and Shell-TPMS designs analyzed in this research were generated with TPMSgen [70] from the corresponding mathematical equation presented below:

$$J \rightarrow \sin(x)\cdot\cos(y)+\sin(y)\cdot\cos(z)+\sin(z)\cdot\cos(x)=1 \tag{A.1}$$

$$K \rightarrow \cos(x)\cdot\cos(y)\cdot\cos(z)+\sin(x)\cdot\sin(y)\cdot\sin(z)=\frac{1}{2} \tag{A.2}$$

$$M \rightarrow \cos(x)+\cos(y)+\cos(z)=\frac{1}{2.5} \tag{A.3}$$

$$N \rightarrow \cos(x)+\cos(y)+\cos(z)=\frac{1}{1.5} \tag{A.4}$$

$$O \rightarrow 2\cdot[\cos(x)\cdot\cos(y)+\cos(y)\cdot\cos(z)+\cos(z)\cdot\cos(x)] - [\cos(2x)+\cos(2y)+\cos(2z)]=1 \tag{A.5}$$

$$P \rightarrow \sin(x)\cdot\cos(y)+\sin(y)\cdot\cos(z)+\sin(z)\cdot\cos(x)=0 \tag{A.6}$$

$$Q \rightarrow \sin(x)\cdot\sin(y)\cdot\sin(z)+\sin(x)\cdot\cos(y)\cdot\cos(z) + \cos(x)\cdot\sin(y)\cdot\cos(z)+\cos(x)\cdot\cos(y)\cdot\sin(z)=0 \tag{A.7}$$

$$R \rightarrow \sin(2x)\cdot\cos(y)\cdot\sin(z)+\sin(x)\cdot\sin(2y)\cdot\cos(z) + \cos(x)\cdot\sin(y)\cdot\sin(2z)-\cos(2x)\cdot\cos(2y) - \cos(2y)\cdot\cos(2z)-\cos(2z)\cdot\cos(2x)+0.3=0 \tag{A.8}$$

$$S \rightarrow 1.1\cdot[\sin(2x)\cdot\cos(y)\cdot\sin(z)+\sin(x)\cdot\sin(2y)\cdot\cos(z) + \cos(x)\cdot\sin(y)\cdot\sin(2z)]-0.2\cdot[\cos(2x)\cdot\cos(2y) + \cos(2y)\cdot\cos(2z)+\cos(2z)\cdot\cos(2x)] - 0.4\cdot[\cos(2x)+\cos(2y)+\cos(2z)]=0 \tag{A.9}$$

$$T \rightarrow \cos(x)+\cos(y)+\cos(z)=0 \tag{A.10}$$

Appendix B. 3D representation of the stiffness tensor

The following steps allow obtaining the graphical representation of the homogenized stiffness tensor ($\boldsymbol{C^H}$) of the RVE of a cellular solid, expressed in Voigt notation and referenced to the global *XYZ* coordinate system.

First, the generalized Hooke's law for continuous media is expressed as:

$$\boldsymbol{\sigma} = \boldsymbol{C^H}\times\boldsymbol{\varepsilon} \tag{B.1}$$

where $\boldsymbol{\sigma}$ and $\boldsymbol{\varepsilon}$ are the stress and strain tensors referenced to the global *XYZ* coordinates, respectively.

A rotation around the *x*-axis (α), *y*-axis (β), and *z*-axis (γ) can be introduced to evaluate the stress and strain tensors $\boldsymbol{\sigma_{\alpha\beta\gamma}}$ and $\boldsymbol{\varepsilon_{\alpha\beta\gamma}}$ as:

$$\begin{aligned}\boldsymbol{\sigma}_{\alpha\beta\gamma} &= \mathbf{L}^{\sigma}_{\alpha\beta\gamma}\times\boldsymbol{\sigma}\\ \boldsymbol{\varepsilon}_{\alpha\beta\gamma} &= \mathbf{L}^{\varepsilon}_{\alpha\beta\gamma}\times\boldsymbol{\varepsilon}\end{aligned} \tag{B.2}$$

where $\boldsymbol{L^{\sigma}_{\alpha\beta\gamma}}$ and $\boldsymbol{L^{\varepsilon}_{\alpha\beta\gamma}}$ are the bond-stress and strains transformation matrices, which are determined from the rotation matrix $\boldsymbol{Q}$ and classical rotation matrices $\boldsymbol{R_x}$, $\boldsymbol{R_y}$, and $\boldsymbol{R_z}$ as detailed in B.3.where:

$$\boldsymbol{L}^{\sigma}_{\alpha\beta\gamma} = \begin{bmatrix} Q_{11}^2 & Q_{12}^2 & Q_{13}^2 & 2Q_{12}Q_{13} & 2Q_{11}Q_{13} & 2Q_{11}Q_{12} \\ Q_{21}^2 & Q_{22}^2 & Q_{yz}^2 & 2Q_{22}Q_{yz} & 2Q_{21}Q_{yz} & 2Q_{21}Q_{22} \\ Q_{31}^2 & Q_{31}^2 & Q_{33}^2 & 2Q_{31}Q_{33} & 2Q_{31}Q_{33} & 2Q_{31}Q_{31} \\ Q_{21}Q_{31} & Q_{22}Q_{31} & Q_{yz}Q_{33} & Q_{22}Q_{33}+Q_{yz}Q_{31} & Q_{21}Q_{33}+Q_{yz}Q_{31} & Q_{21}Q_{31}+Q_{22}Q_{31} \\ Q_{11}Q_{31} & Q_{12}Q_{31} & Q_{13}Q_{33} & Q_{12}Q_{33}+Q_{13}Q_{31} & Q_{11}Q_{33}+Q_{13}Q_{31} & Q_{11}Q_{31}+Q_{12}Q_{31} \\ Q_{11}Q_{21} & Q_{12}Q_{22} & Q_{13}Q_{yz} & Q_{12}Q_{yz}+Q_{13}Q_{22} & Q_{11}Q_{yz}+Q_{13}Q_{21} & Q_{11}Q_{22}+Q_{12}Q_{21} \end{bmatrix}$$

$$\boldsymbol{L}^{\varepsilon}_{\alpha\beta\gamma} = \begin{bmatrix} Q_{11}^2 & Q_{12}^2 & Q_{13}^2 & Q_{12}Q_{13} & Q_{11}Q_{13} & Q_{11}Q_{12} \\ Q_{21}^2 & Q_{22}^2 & Q_{yz}^2 & Q_{22}Q_{yz} & Q_{21}Q_{yz} & Q_{21}Q_{22} \\ Q_{31}^2 & Q_{31}^2 & Q_{33}^2 & Q_{31}Q_{33} & Q_{31}Q_{33} & Q_{31}Q_{31} \\ 2Q_{21}Q_{31} & 2Q_{22}Q_{31} & 2Q_{yz}Q_{33} & Q_{22}Q_{33}+Q_{yz}Q_{31} & Q_{21}Q_{33}+Q_{yz}Q_{31} & Q_{21}Q_{31}+Q_{22}Q_{31} \\ 2Q_{11}Q_{31} & 2Q_{12}Q_{31} & 2Q_{13}Q_{33} & Q_{12}Q_{33}+Q_{13}Q_{31} & Q_{11}Q_{33}+Q_{13}Q_{31} & Q_{11}Q_{31}+Q_{12}Q_{31} \\ 2Q_{11}Q_{21} & 2Q_{12}Q_{22} & 2Q_{13}Q_{yz} & Q_{12}Q_{yz}+Q_{13}Q_{22} & Q_{11}Q_{yz}+Q_{13}Q_{21} & Q_{11}Q_{22}+Q_{12}Q_{21} \end{bmatrix} \tag{B.3}$$

$\boldsymbol{Q_{ij}}$ corresponds to the element located in row i and column j in $\boldsymbol{Q}$.

$$\boldsymbol{Q} = \boldsymbol{R_x} \times \boldsymbol{R_y} \times \boldsymbol{R_z}$$

$$\boldsymbol{R_x}(\alpha) = \begin{bmatrix} 1 & 0 & 0 \\ 0 & \cos(\alpha) & -\sin(\alpha) \\ 0 & \sin(\alpha) & \cos(\alpha) \end{bmatrix}$$

$$\boldsymbol{R_y}(\beta) = \begin{bmatrix} \cos(\beta) & 0 & \sin(\beta) \\ 0 & 1 & 0 \\ -\sin(\beta) & 0 & \cos(\beta) \end{bmatrix} \quad \boldsymbol{R_z}(\gamma) = \begin{bmatrix} \cos(\gamma) & -\sin(\gamma) & 0 \\ \sin(\gamma) & \cos(\gamma) & 0 \\ 0 & 0 & 1 \end{bmatrix}$$

Substituting Eqs. (B.2) into Eq. (B.1), the following expression Eq. (B.4) is obtained:

$$\sigma_{\alpha\beta\gamma} = L^{\sigma}_{\alpha\beta\gamma} \times C^{H} \times L^{\varepsilon-1}_{\alpha\beta\gamma} \times \varepsilon_{\alpha\beta\gamma} \tag{B.4}$$

Then, the effective stiffness tensor in a specific orientation ($\boldsymbol{C^H_{\alpha\beta\gamma}}$) can be determined as:

$$C^{H}_{\alpha\beta\gamma} = L^{\sigma}_{\alpha\beta\gamma} \times C^{H} \times L^{\varepsilon-1}_{\alpha\beta\gamma} \tag{B.5}$$

At this point, the corresponding compliance tensor $\boldsymbol{S^H_{\alpha\beta\gamma}}$ can be directly calculated by inverting $\boldsymbol{C^H_{\alpha\beta\gamma}}$. Thus, for example, taking the global x-axis reference, the effective Young's modulus $E_{\alpha\beta\gamma}$ is:

$$E_{\alpha\beta\gamma} = \frac{1}{S^{H}_{\alpha\beta\gamma 11}} \tag{B.6}$$

where $S^{H}_{\alpha\beta\gamma 11}$ is the first term of the effective compliance tensor $\boldsymbol{S^H_{\alpha\beta\gamma}}$.

Finally, the graphical representation of the homogenized stiffness tensor can be plotted with the sequential computation of different rotation angles α, β, and γ. Each combination will rotate the tensor and evaluate the effective stiffness in a particular examined direction $d_{\alpha\beta\gamma}$:

$$\boldsymbol{d_{\alpha\beta\gamma}} = \boldsymbol{Q} \times \begin{bmatrix} 1 \\ 0 \\ 0 \end{bmatrix} \tag{B.7}$$

Accordingly, given an orientation $\boldsymbol{d_{\alpha\beta\gamma}}$ and the corresponding effective Young's modulus $E_{\alpha\beta\gamma}$, the coordinates x , y, and z, of a point in the graphical representation of the stiffness tensor are obtained as:

$$\begin{cases} x = E_{\alpha\beta\gamma}.d_{\alpha\beta\gamma 1} \\ y = E_{\alpha\beta\gamma}.d_{\alpha\beta\gamma 2} \\ z = E_{\alpha\beta\gamma}.d_{\alpha\beta\gamma 3} \end{cases} \tag{B.8}$$

References

[1] L.J. Gibson, M.F. Ashby. Cellular solids - Structure and properties. Cambridge University Press, 2n edition edition, 1997. ISBN 0-521-49911-9. URL https://doi.org/10.1017/CBO9781139878326.

[2] Y. Liu and H. Hu. A review on auxetic structures and polymeric materials. *Sci. Res. Essays*, 5(10):1052–1063, 2010. ISSN 1992-2248. URL https://doi.org/10.5897/SRE.9000104.

[3] J.C. Álvarez-Elipe, A. Díaz-Lantada, Comparative study of auxetic geometries by means of computer-aided design and engineering, Smart Mater. Struct. 21 (2012) 0964–1726, https://doi.org/10.1088/0964-1726/21/10/105004.

[4] N. A. Fleck, V. S. Deshpande, and M. F. Ashby. Micro-architectured materials: past, present and future, Proc. R. Soc. A 466(2121):2495–2516, 2010. ISSN 1364-5021. URL https://doi.org/10.1098/rspa.2010.0215.

[5] K. Refai, M. Montemurro, C. Brugger, N. Saintier, Determination of the effective elastic properties of titanium lattice structures, Mech. Adv. Mater. Struct. 27 (2020) 1537–6494, https://doi.org/10.1080/15376494.2018.1536816.

[6] Q. Liu, R. Xu, Y. Zhou, J. Ge, S. Yuan, Y. Long, and T. Shi. Metamaterials mapped lightweight structures by principal stress lines and topology optimization: Methodology, additive manufacturing, ductile failure and tests. Mater. Des. 212:110192, 2021. ISSN 0264-1275. URL https://doi.org/10.1016/j.matdes.2021.110192.

[7] L. Cheng, J. Bai, A.C. To. Functionally graded lattice structure topology optimization for the design of additive manufactured components with stress constraints. Comput. Methods Appl. Mech. Eng., 344:334–359, 2019. ISSN 0045-7825. URL https://doi.org/10.1016/j.cma.2018.10.010.

[8] J. Aquino, I. Duarte, J. Dias-de Oliveira, Modelling and effective properties prediction of metal foams, Sci. Tech. Mater., 30(1), 43–49, 2018. ISSN 2603-6363. URL https://doi.org/10.1016/j.stmat.2018.01.004.

[9] Y. Feng, T. Huang, Y. Gong, P. Jia. Stiffness optimization design for TPMS architected cellular materials, Mater. Des. 222: 111078, 2022. ISSN 1873-4197. URL https://doi.org/10.1016/j.matdes.2022.111078.

[10] N. Yang, H. Wei, and Z. Mao. Tuning surface curvatures and young's moduli of TPMS-based lattices independent of volume fraction. *Mater. Design*, 216:110542, 2022. ISSN 1873-4197. URL https://doi.org/10.1016/j.matdes.2022.110542.

[11] C. Lin, G. Wen, H. Yin, Z.-P. Wang, J. Liu, Y.M. Xie, Revealing the sound insulation capacities of TPMS sandwich panels, J. Sound Vib. 540 (2022) 117303.

[12] C. Zeng, W. Wang, Modeling method for variable and isotropic permeability design of porous material based on TPMS lattices, Tribol. Int. 176 (2022) 107913.

[13] S. Pramanik, D. Milaege, K.-P. Hoyer, M. Schaper, Additively manufactured novel Ti6Al7Nb circular honeycomb cellular solid for energy absorbing applications, Mater. Sci. Eng. A 854 (2022), https://doi.org/10.1016/j.msea.2022.143887 143887.

[14] J. W. Lee, S. H. Oh, E. Jeon, J. Kim, and K. Park. Functional gradation of the morphological properties of TPMS channel for enhanced flow performance, Mater. Des. 224:111413, 2022. ISSN 1873-4197. URL https://doi.org/10.1016/j.matdes.2022.111413.

[15] N. Novak, D. Kytyr, V. Rada, T. Doktor, O. Al-Ketan, R. Rowshan, M. Vesenjak, Z. Ren, Compression behaviour of TPMS-filled stainless steel tubes, Mater. Sci. Eng. A, 852:143680, 2022. ISSN 0921-5093. URL https://doi.org/10.1016/j.msea.2022.143680.
[16] K. Wei, X. Xiao, J. Chen, Y. Wu, M. Li, and Z. Wang. Additively manufactured bi-material metamaterial to program a wide range of thermal expansion, Mater. Des. 198:109343, 2021. ISSN 0264-1275. URL https://doi.org/10.1016/j.matdes.2020.109343.
[17] Y. L. Tee, T. Maconachie, P. Pille, M. Leary, T. Do, P. Tran, From nature to additive manufacturing: biomimicry of porcupine quill, Mater. Des. 210:110041, 2021. ISSN 0264-1275. URL https://doi.org/10.1016/j.matdes.2021.110041.
[18] M. Ouda, O. Al-Ketan, N. Sreedhar, M.I. Hasan Ali, R.K. Abu Al-Rub, S. Hong, H.A. Arafat, Novel static mixers based on triply periodic minimal surface (TPMS) architectures, J. Environ Chem. Eng. 8 (2020) 2213–2929, https://doi.org/10.1016/j.jece.2020.104289.
[19] C. Yang, Q.M. Li. Advanced lattice material with high energy absorption based on topology optimisation, Mech. Mater. 148:103536, 2020. ISSN 0167-6636. URL https://doi.org/10.1016/j.mechmat.2020.103536.
[20] Y. Xu, D. Zhang, S. Hu, R. Chen, Y. Gu, X. Kong, J. Tao, Y. Jiang, Mechanical properties tailoring of topology optimized and selective laser melting fabricated Ti6Al4V lattice structure, J. Mech. Behav. Biomed. Mater. 99 (2019) 225–239. ISSN 1751-6161. URL https://doi.org/10.1016/j.jmbbm.2019.06.021.
[21] Z. Qin, G. S. Jung, M. J. Kang, M.J. Buehler, The mechanics and design of a lightweight three-dimensional graphene assembly, Sci. Adv, 3(1) (2017) 1–9. ISSN 2375-2548. URL https://doi.org/10.1126/sciadv.1601536.
[22] J.A. Gopsill, J. Shindler, B.J. Hicks, Using finite element analysis to influence the infill design of fused deposition modelled parts, Prog. Addit. Manuf., 3 (2018) 145–163. ISSN 2363-9520. URL https://doi.org/10.1007/s40964-017-0034-y.
[23] C.O. Ufodike, H. Wang, M.F. Ahmed, G. Dolzyk, S. Jung, Design and modeling of bamboo biomorphic structure for in-plane energy absorption improvement, Mater. Des. 205 (2021) 109736. ISSN 0264-1275. URL https://doi.org/10.1016/j.matdes.2021.109736.
[24] L. Bai, Y. Xu, X. Chen, L. Xin, J. Zhang, K. Li, Y. Sun. Improved mechanical properties and energy absorption of Ti6Al4V laser powder bed fusion lattice structures using curving lattice struts, Mater. Des. 211:110140, 2021. ISSN 0264-1275. URL https://doi.org/10.1016/j.matdes.2021.110140.
[25] G. Ye, H. Bi, Y. Hu, Compression behaviors of 3D printed pyramidal lattice truss composite structures, Compos. Struct. 233 (2020) 111706. ISSN 0263-8223. URL https://doi.org/10.1016/j.compstruct.2019.111706.
[26] A. Arjunan, M. Singh, A. Baroutaji, C. Wang. Additively manufactured AlSi10Mg inherently stable thin and thick-walled lattice with negative Poisson's ratio, Compos. Struct. 247 (2020) 112469. ISSN 0263-8223. URL https://doi.org/10.1016/j.compstruct.2020.112469.
[27] B. Bahrami Babamiri, H. Askari, K. Hazeli, Deformation mechanisms and post-yielding behavior of additively manufactured lattice structures, Mater. Des. 188 (2020) 108443. ISSN 0264-1275. URL https://doi.org/10.1016/j.matdes.2019.108443.
[28] L. Azzouz, Y. Chen, M. Zarrelli, J. M. Pearce, L. Mitchell, G. Ren, M. Grasso. Mechanical properties of 3-D printed truss-like lattice biopolymer non-stochastic structures for sandwich panels with natural fibre composite skins, Compos. Struct. 213 (2019) 220–230. ISSN 0263-8223. URL https://doi.org/10.1016/j.compstruct.2019.01.103.
[29] X. Y. Zhang, G. Fang, L. L. Xing, W. Liu, J. Zhou, Effect of porosity variation strategy on the performance of functionally graded Ti-6Al-4V scaffolds for bone tissue engineering, Mater. Des. 157, 523–538, 2018. ISSN 0264-1275. URL https://doi.org/10.1016/j.matdes.2018.07.064.
[30] S. R. G. Bates, I. R. Farrow, and R. S. Trask. 3D printed elastic honeycombs with graded density for tailorable energy absorption. In: SPIE Smart Structures and Materials + Nondestructive Evaluation and Health Monitoring, Las Vegas, NV, 2016. URL https://doi.org/10.1117/12.2219322.
[31] Y.L. Yap, W.Y. Yeong, Shape recovery effect of 3D printed polymeric honeycomb: this paper studies the elastic behaviour of different honeycomb structures produced by PolyJet technology, Virtual Phys. Prototyp. 10 (2015) 1745–2767, https://doi.org/10.1080/17452759.2015.1060350.
[32] X. Chen, M. Hu, Y. Sun, J. Yang, L. Bai, Y. Xiong. Wide-range tuning of the mechanical properties of TPMS lattice structures through frequency variation, Mater. Des. 224 (2022) 111370. ISSN 0264-1275. URL https://doi.org/10.1016/j.matdes.2022.111370.
[33] J. Fu, P. Sun, Y. Du, H. Li, X. Zhou, Q. Tian, Isotropic design and mechanical characterization of TPMS-based hollow cellular structures, Compos. Struct. 279 (2022), https://doi.org/10.1016/j.compstruct.2021.114818 114818.
[34] X. Yang, Q.Y.Y. Shi, L. Yang, S. Wu, C. Yan, Y. Shi, Effect of volume fraction and unit cell size on manufacturability and compressive behaviors of Ni-Ti triply periodic minimal surface lattices, Addit. Manuf. 54 (2022) 102737.
[35] A. Jones, M. Leary, S. Bateman, M. Easton, Parametric design and evaluation of TPMS-like cellular solids, Mater. Des. 221 (2022) 110908, 2022. ISSN 1873-4197. URL https://doi.org/10.1016/j.matdes.2022.110908.
[36] Z. Alomar, F. Concli, Compressive behavior assessment of a newly developed circular cell-based lattice structure, Mater. Des. 205 (2021) 109716, ISSN 0264-1275. URL https://doi.org/10.1016/j.matdes.2021.109716.
[37] R. Ding, J. Yao, B. Du, L. Zhao, Y. Guo, Mechanical properties and energy absorption capability of ARCH lattice structures manufactured by selective laser melting, Adv. Eng. Mater. 22 (2020) 1438–1656, https://doi.org/10.1002/adem.201901534.
[38] C. Li, H. Lei, Y. Liu, X. Zhang, J. Xiong, H. Zhou, D. Fang, Crushing behavior of multi-layer metal lattice panel fabricated by selective laser melting, Int. J. Mech. Sci. 145 (2018) 389–399. ISSN 00207403. URL https://doi.org/10.1016/j.ijmecsci.2018.07.029.
[39] Z. Xiao, Y. Yang, R. Xiao, Y. Bai, C. Song, D. Wang. Evaluation of topology-optimized lattice structures manufactured via selective laser melting, Mater. Des. 143 (2018) 27–37. ISSN 0264-1275. URL https://doi.org/10.1016/j.matdes.2018.01.023.
[40] X. Cao, S. Duan, J. Liang, W. Wen, D. Fang, Mechanical properties of an improved 3D-printed rhombic dodecahedron stainless steel lattice structure of variable cross section, Int. J. Mech. Sci. 145 (2018) 53–63, ISSN 0020-7403. URL https://doi.org/10.1016/j.ijmecsci.2018.07.006.
[41] R. Gümrük, R.A. Mines, S. Karadeniz, Static mechanical behaviours of stainless steel micro-lattice structures under different loading conditions, Mater. Sci. Eng. A 586 (2013) 392–406. ISSN 0921-5093. URL https://doi.org/10.1016/j.msea.2013.07.070.
[42] R. Alberdi, R. Dingreville, J. Robbins, T. Walsh, B. C. White, B. Jared, B.L. Boyce, Multi-morphology lattices lead to improved plastic energy absorption, Mater. Des. 194 (2020) 108883. ISSN 0264-1275. URL https://doi.org/10.1016/j.matdes.2020.108883.
[43] C. Li, H. Lei, Z. Zhang, X. Zhang, H. Zhou, P. Wang, and D. Fang. Architecture design of periodic truss-lattice cells for additive manufacturing. Addit. Manuf. 34 (2020) 101172. ISSN 2214-8604. URL https://doi.org/10.1016/j.addma.2020.101172.
[44] T. Maconachie, M. Leary, B. Lozanovski, X. Zhang, M. Qian, O. Faruque, M. Brandt. SLM lattice structures: properties, performance, applications and challenges, Mater. Des. 183:108137, 2019. ISSN 0264-1275. URL https://doi.org/10.1016/j.matdes.2019.108137.
[45] A.M. Torres, A.A. Trikanad, C.A. Aubin, F.M. Lambers, M. Luna, C.M. Rimnac, P. Zavattieri, C.J. Hernandez, Bone-inspired microarchitectures achieve enhanced fatigue life, Proc. Natl. Acad. Sci. U.S.A. 116 (2019) 0027–8424, https://doi.org/10.1073/pnas.1905814116.
[46] F. N. Habib, P. Iovenitti, S. H. Masood, M. Nikzad, Fabrication of polymeric lattice structures for optimum energy absorption using Multi Jet Fusion technology, Mater. Des. 155 (2018) 86–98. ISSN 0264-1275. URL https://doi.org/10.1016/j.matdes.2018.05.059.
[47] M. Leary, M. Mazur, H. Williams, E. Yang, A. Alghamdi, B. Lozanovski, X. Zhang, D. Shidid, L. Farahbod-Sternahl, G. Witt, I. Kelbassa, P. Choong, M. Qian, M. Brandt, Inconel 625 lattice structures manufactured by selective laser melting (SLM): Mechanical properties, deformation and failure modes, Mater. Des. 157 (2018) 179–199. ISSN 0264-1275. URL https://doi.org/10.1016/j.matdes.2018.06.010.
[48] L. Yang, O. Harrysson, D. Cormier, H. West, H. Gong, B. Stucker, Additive manufacturing of metal cellular structures: design and fabrication, Jom 67(3) (2015) 608–615, ISSN 1543-1851. URL https://doi.org/10.1007/s11837-015-1322-y.
[49] J. J. Andrew, H. Alhashmi, A. Schiffer, S. Kumar, V.S. Deshpande, Energy absorption and self-sensing performance of 3D printed CF/PEEK cellular composites, Mater. Des. 208 (2021) 109863. ISSN 0264-1275. URL https://doi.org/10.1016/j.matdes.2021.109863.
[50] S.M. Zaharia, L.A. Enescu, M.A. Pop, Mechanical performances of lightweight sandwich structures produced by material extrusion-based additive manufacturing, Polymers 12 (2020), https://doi.org/10.3390/polym12081740.
[51] Y. Tao, L. Pan, D. Liu, P. Li, A case study: Mechanical modeling optimization of cellular structure fabricated using wood flour-filled polylactic acid composites with fused deposition modelling, Compos. Struct. 216 (2019) 360–365. ISSN 0263-8223. URL https://doi.org/10.1016/j.compstruct.2019.03.010.
[52] A. Kumar, S. Verma, J.-Y. Jeng, Supportless lattice structures for energy absorption fabricated by fused deposition modelling, 3D Print Addit Manuf. 7 (2020) 2329–7662, https://doi.org/10.1089/3dp.2019.0089.
[53] J. D. Rossiter, A. A. Johnson, G.A. Bingham, Assessing the design and compressive performance of material extruded lattice structures, 3D Print Addit Manuf, 7(1) (2020) 19–27, ISSN 2329-7662, URL https://doi.org/10.1089/3dp.2019.0030.
[54] A. Forés-Garriga, G. Gómez-Gras, M. A. Pérez, Mechanical performance of additively manufactured lightweight cellular solids: influence of cell pattern and relative density on the printing time and compression behaviour, Mater. Design 215 (2022) 110474. ISSN 0264-1275. URL https://doi.org/10.1016/j.matdes.2022.110474.
[55] Y. Lu, W. Zhao, Z. Cui, H. Zhu, C. Wu, The anisotropic elastic behavior of the widely-used triply-periodic minimal surface based scaffolds, J. Mech. Behav. Biomed. Mater. 99(2) (2019) 56–65. ISSN 18780180. URL https://doi.org/10.1016/j.jmbbm.2019.07.012.
[56] W. Liu, H. Song, Z. Wang, J. Wang, C. Huang, Improving mechanical performance of fused deposition modeling lattice structures by a snap-fitting method, Mater. Des. 181 (2019) 108065, ISSN 0264-1275, URL https://doi.org/10.1016/j.matdes.2019.108065.
[57] G. Dong, G. Wijaya, Y. Tang, Y. F. Zhao, Optimizing process parameters of fused deposition modeling by Taguchi method for the fabrication of lattice structures, Addit. Manuf., 19 (2018) 62–72, ISSN 2214-8604, URL https://doi.org/10.1016/j.addma.2017.11.004.
[58] R. Gautam, S. Idapalapati, S. Feih, Printing and characterisation of Kagome lattice structures by fused deposition modelling, Mater. Design, 137 (2018) 266–275, ISSN 0264-1275, URL https://doi.org/10.1016/j.matdes.2017.10.022.
[59] N. Sreedhar, N. Thomas, O. Al-Ketan, R. Rowshan, H.H. Hernandez, R.K. Abu Al-Rub, H.A. Arafat. Mass transfer analysis of ultrafiltration using spacers based

on triply periodic minimal surfaces: Effects of spacer design, directionality and voidage, J. Membr. Sci., 561 (2018) 89–98, ISSN 0376-7388, URL https://doi.org/10.1016/j.memsci.2018.05.028.
[60] O. Al-Ketan, R. Rezgui, R. Rowshan, H. Du, N. X. Fang, R.K. Abu Al-Rub, Microarchitected stretching-dominated mechanical metamaterials with minimal surface topologies, Adv. Eng. Mater. 20(9) (2018) 1800029, ISSN 15272648. URL https://doi.org/10.1002/adem.201800029.
[61] O. Al-Ketan, D. W. Lee, R. Rowshan, R. K. Abu Al-Rub, Functionally graded and multi-morphology sheet TPMS lattices: Design, manufacturing, and mechanical properties, J. Mech. Behav. Biomed. Mater., 102 (2020) 103520, ISSN 1751-6161, URL https://doi.org/10.1016/j.jmbbm.2019.103520.
[62] N. Sathishkumar, N. Vivekanandan, L.Balamurugan, N. Arunkumar, I. Ahamed, Mechanical properties of triply periodic minimal surface based lattices made by polyjet printing, Mater. Today: Proc., 22(4) (2020) 2934–2940, ISSN 2214-7853, URL https://doi.org/10.1016/j.matpr.2020.03.427.
[63] H. Jia, H. Lei, P. Wang, J. Meng, C. Li, H. Zhou, X. Zhang, D. Fang, An experimental and numerical investigation of compressive response of designed Schwarz Primitive triply periodic minimal surface with non-uniform shell thickness, Extreme Mech. Lett. 37 (2020) 100671, ISSN 2352-4316, URL https://doi.org/10.1016/j.eml.2020.100671.
[64] A. Kumar, L. Collini, A. Daurel, J.Y. Jeng, Design and additive manufacturing of closed cells from supportless lattice structure, Addit. Manuf., 33(January) (2020) 101168, ISSN 2214-8604. URL https://doi.org/10.1016/j.addma.2020.101168.
[65] D. Downing, A. Jones, M. Brandt, M. Leary, Increased efficiency gyroid structures by tailored material distribution, Mater. Des. 197 (2021) 109096, ISSN 0264-1275. URL https://doi.org/10.1016/j.matdes.2020.109096.
[66] I. Maskery, N. T. Aboulkhair, A. O. Aremu, C.J. Tuck, I.A. Ashcroft, Compressive failure modes and energy absorption in additively manufactured double gyroid lattices, Addit. Manuf 16 (2017) 24–29, ISSN 2214-8604, URL https://doi.org/10.1016/j.addma.2017.04.003.
[67] A. Forés-Garriga, H. García de la Torre, R. Lado-Roigé, G. Gómez- Gras, and M.A. Pérez. Triply Periodic Minimal Surfaces Generator - TPMSgen (2023). URL https://github.com/albertforesg/TPMSgen.
[68] A. Forés-Garriga, M. A. Pérez, G. Gómez-Gras, G. Reyes-Pozo. Role of infill parameters on the mechanical performance and weight reduction of PEI Ultem processed by FFF, Mater. Des. 193 (2020) 108810, ISSN 1873-4197, URL https://doi.org/10.1016/j.matdes.2020.108810.
[69] A. Chueca de Bruijn, G. Gómez-Gras, M. A. Pérez, Selective dissolution of polysulfone support material of fused filament fabricated Ultem 9085 parts, Polym. Test., 108 (2022) 107495, ISSN 01429418, URL https://doi.org/10.1016/j.polymertesting.2022.107495.
[70] A. Chueca de Bruijn, G. Gómez-Gras, M.A. Pérez, Mechanical study on the impact of an efective solvent support-removal methodology for FDM Ultem 9085 parts, Polym. Test., page 106702, 2020. ISSN 0893-9659. URL https://doi.org/10.1016/j.polymertesting.2020.106433.
[71] ASTM C365: Standard Test Method for Flatwise Compressive Properties of Sandwich Cores. Technical report, ASTM International, 2016. URL https://doi.org/10.1520/C0365_C0365M-16.
[72] M.M. Pastor-Artigues, F. Roure-Fernández, X. Ayneto-Gubert, J. Bonada-Bo, E. Pérez-Guindal, I. Buj-Corral, Elastic asymmetry of PLA material in FDM-printed parts: Considerations concerning experimental characterisation for use in numerical simulations, Materials 13(15) (2020) 1–24, ISSN 1996-1944, URL https://doi.org/10.3390/ma13010015.
[73] O. Fashanu, D. Murphy, M. Spratt, J. Newkirk, K. Chandrashekhara, B. Brown, J. Porter, Effective elastic properties of additively manufactured metallic cellular structures using numerical unit-cell homogenization, Prog. Addit. Manuf., 5 (2020) 355–366, ISSN 2363-9520, URL https://doi.org/10.1007/s40964-020-00141-7.
[74] D. V. Grinevich, N.O. Yakovlev, P.B. Mazalov, Linear homogenization in the analysis of cellular structures produced by additive technology, Russ. Eng. Res. 41 (2021) 423–427, ISSN 1068-798X, URL https://doi.org/10.3103/S1068798X2105004X.
[75] C.M. Zener, S. Siegel, Elasticity and anelasticity of metals, J. Phys. Chem. 53 (9) (1949) 1468, https://doi.org/10.1021/j150474a017.
[76] S.I. Ranganathan, M. Ostoja-Starzewski, Universal elastic anisotropy index, Phys. Rev. Lett., 101(5) (2008) 055504, ISSN 0031-9007, URL https://doi.org/10.1103/PhysRevLett.101.055504.
[77] J. Fu, P. Sun, Y. Du, H. Li, X. Zhou, Q. Tian, Isotropic design and mechanical characterization of TPMS-based hollow cellular structures, Compos. Struct., 279:114818, 2022. ISSN 0263-8223, URL https://doi.org/10.1016/j.compstruct.2021.114818.
[78] C. Lubombo, M.A. Huneault, Effect of infill patterns on the mechanical performance of lightweight 3D-printed cellular PLA parts, Mater. Today Commun. 17 (2018) 214–228, ISSN 2352-4928, URL https://doi.org/10.1016/j.mtcomm.2018.09.017.
[79] J. M. Chacón, M. A. Caminero, E. García-Plaza, P.J. Núñez, Additive manufacturing of PLA structures using fused deposition modelling: effect of process parameters on mechanical properties and their optimal selection, Mater. Des. 124 (2017) 143–157, ISSN 0264-1275, doi: 10.1016/j.matdes.2017.03.065.
[80] ASTM D790-17, Standard Test Methods for Flexural Properties of Unreinforced and Reinforced Plastics and Electrical Insulating Materials. Technical report, ASTM International, 2017. URL https://doi.org/10.1520/D0790-17.
[81] Stratasys. ULTEM^{TM} 9085 Resin FDM Thermoplastic Filament Fit for High-Performance Applications. Technical report; 2021. URL https://support.stratasys.com/en/materials/fdm/ultem-9085.